
PHYSICS AND ASTRONOMY

TRACK: GRAVITATION AND ASTROPARTICLE PHYSICS AMSTERDAM

MASTER PROJECT

60 EC

Branching fraction measurement of $\Lambda_b^0 \rightarrow J/\psi \Lambda$

Author:
Vlad Dedu
12392286

Supervisors:
Dr. Niels Tuning
Mick Mulder
Lex Greeven

Second examiner:
Prof. dr. Patrick
Decowski

November 16, 2020

Abstract

In this thesis, the first measurement of the branching fraction $\mathcal{B}(\Lambda_b^0 \rightarrow J/\psi \Lambda)$ at the LHC is presented. The measurement uses the full Run 2 proton-proton data collected with the LHCb detector at $\sqrt{s} = 13$ TeV. Using the decay $B^0 \rightarrow J/\psi K_S^0$ as a normalisation channel, the measurement is reported to be $\mathcal{B}(\Lambda_b^0 \rightarrow J/\psi \Lambda) = (2.67 \pm 0.03 \text{ (stat.)} \pm 0.20 \text{ (external syst.)}) \times 10^{-4}$, excluding experimental systematic uncertainties. This is the most precise measurement to date with an uncertainty improved by more than a factor three compared to previous estimations. The improved precision on $\mathcal{B}(\Lambda_b^0 \rightarrow J/\psi \Lambda)$ will significantly reduce the uncertainties for the measurement of the branching fraction $\mathcal{B}(\Lambda_b^0 \rightarrow \Lambda \mu^+ \mu^-)$ and search for the Lepton Flavour Violating decay $\mathcal{B}(\Lambda_b^0 \rightarrow \Lambda e^\pm \mu^\mp)$, for both of which $\Lambda_b^0 \rightarrow J/\psi \Lambda$ is used as a normalisation channel.

Acknowledgements

First of all, I want to express my gratitude to my supervisors Niels Tuning, Mick Mulder and Lex Greeven. Niels, even though you were very busy, you always made time for the weekly meetings and attended my presentations. Your feedback and the discussions we had on the analysis were very helpful and enjoyable. Your support, not just in my work but in all matters, throughout the entire project, helped me a lot to stay motivated. In general, I believe my performance in this project greatly benefited from your positivity and support. Mick, a huge thank you goes to you for all the different ways in which you helped me. Although you were doing your work as well as writing on your PhD thesis, you always had time to answer my questions. Our daily discussions helped me understand the physics concepts and methods we use in the analysis and helped me make constant progress. You always checked if I was stuck with something and always offered to provide help, sometimes even without me asking for it. You made the work environment very comfortable and pleasant and made sure everything stays on track with the analysis, but also on a personal level. I have learned a lot from you during this project and I greatly appreciate all your support. Lex, as a daily supervisor, you were always there to help me. During most of the project, as you were present at Nikhef, you always came to the master students office and checked how my work was going. After all meetings moved online due to the coronavirus pandemic, you always made time to discuss any issues I was having. You were always able to help me with the code issues I encountered and give advice on how to improve my code. Thank you for reading this thesis several times and giving important feedback. In general, I was very lucky to have you as my supervisors and you all greatly inspired me.

Secondly, I want to thank everybody in the LHCb group at Nikhef, for creating a pleasant environment to work in and for all the help they provided. In particular, I thank Sevda Esen and Maarten van Veghel for their comments and explanations on some aspects of the analysis. Special thanks goes to the other fellow master students I shared the office with: Koen, Bas and Ali. You made the work hours much more fun and enjoyable.

Last but not least I want to thank my family and friends for all their support during my master project.

Contents

1	Introduction	1
1.1	Motivation	1
1.2	Analysis Strategy	4
2	The LHCb detector at the Large Hadron Collider	7
2.1	LHC	7
2.2	The LHCb detector	7
3	Data flow and event selection in Run 2	11
3.1	Trigger selection	11
3.2	Stripping selection	12
3.3	Offline selection/Preselection	13
4	Mass fit model and signal yield extraction	17
4.1	Signal shape	18
4.2	Modelling of peaking backgrounds	19
4.3	Combinatorial background	21
4.4	Fit results	21
5	Efficiencies and MC-data corrections	24
5.1	$B^0 \rightarrow J/\psi K_S^0$ kinematic reweighting	25
5.2	$\Lambda_b^0 \rightarrow J/\psi \Lambda$ kinematic reweighting	25
5.3	Efficiencies	28
6	Results	32
6.1	Systematic uncertainties	33
7	Conclusion and outlook	35
7.1	Outlook	35
A	Preselection plots	40
B	Fit Monte-Carlo templates	42
C	Rewighted variables $\Lambda_b^0 \rightarrow J/\psi \Lambda$	43
D	Rewighted variables $B^0 \rightarrow J/\psi K_S^0$	46

1 Introduction

1.1 Motivation

The Standard Model (SM) [1–3] of particle physics is a model in which particles are described in terms of quantum fields, and so far it has been very successful in describing all known particles and the interactions between them. The particles that make up all matter, and their antimatter counterparts, are called fermions, and they consist of quarks and leptons. The fermions come into three generations of doublets. Quarks can be classified into up-type and down-type quarks in three generations: up (u) and down (d), charm (c) and strange (s) and top (t) and bottom (b). Similarly, the three generations of leptons can be classified as: electron (e^-) and electron neutrino (ν_e), muon (μ^-) and muon neutrino ν_μ and tau (τ^-) and tau neutrino (ν_τ). All six quarks and six leptons have their own antiparticles with the same mass but opposite quantum numbers and, except neutrinos, opposite charge, resulting in 24 fundamental fermions. Baryons are particles composed of three quarks, such as the Λ_b^0 baryon which consists of a udb triplet, while the Λ baryon is composed of a uds quark triplet. Mesons are particles made out of a quark and antiquark, such as the J/ψ meson which is composed of a $c\bar{c}$ quark pair. Within the SM, the interaction between fermions is mediated by boson fields. The gauge bosons are spin-1 particles that mediate the different types of interactions as follows: massless photons (γ) mediate electromagnetic interaction between charged particles, the massive W^+ , W^- , Z bosons mediate the weak interaction between particles with flavour (leptons and quarks) and the massless gluons (g) mediate the strong interaction between particles that have color charge (quarks). In addition, the massive scalar Higgs boson is responsible for the mechanism through which the massive bosons and fermions acquire mass. All the fundamental particles in the SM are schematically presented in Figure 1 along with their properties such as mass, charge and spin.

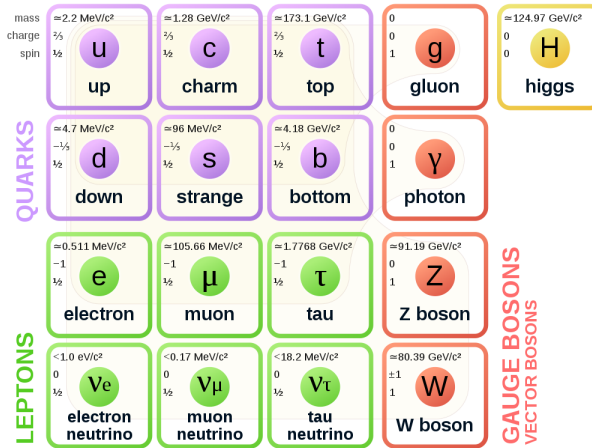


Figure 1: Fundamental particles in the Standard Model and their properties. Figure taken from [4]

Excluding gravity, there are three fundamental forces in the SM, namely the electromagnetic force, the weak force and the strong force. The weak interaction is the

only interaction that can change the flavour of a quark, i.e. quark mixing. The mixing between different generations comes as a result of the Yukawa couplings of fermion fields with the Higgs field, which are added ad-hoc in the SM Lagrangian. The couplings of quark mixing between different generations are given by the elements of the unitary 3×3 Cabbibo-Kobayashi-Maskawa (CKM) matrix. The CKM matrix contains a (weak) complex phase which gives rise to CP-violation. The couplings from the CKM matrix favor transitions between up-type and down-type quarks from the same generation, but highly suppress transitions between quarks of different generations.

In the SM, tree-level quark flavour mixing only occurs through the exchange of charged W^\pm bosons, i.e. charged currents. Consequently, there are no flavour changing neutral currents (FCNC) at tree level in the SM. An example of this type of transition, which changes the quark flavour without altering the charge, is the $b \rightarrow s$ transition which can be studied using the $\Lambda_b^0 \rightarrow \Lambda \mu^+ \mu^-$ decay. One possible loop Feynman diagram of the $\Lambda_b^0 \rightarrow \Lambda \mu^+ \mu^-$ decay is shown in Figure 2.

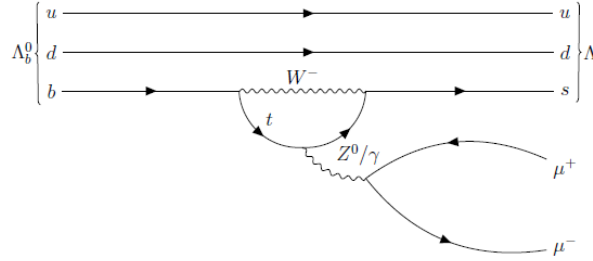


Figure 2: An example loop diagram of the $\Lambda_b^0 \rightarrow \Lambda \mu^+ \mu^-$ decay. Figure taken from [5]

As the $\Lambda_b^0 \rightarrow \Lambda \mu^+ \mu^-$ decay is a FCNC process that can only occur via higher order diagrams, it is a very rare decay being heavily suppressed by the presence of multiple vertices and by the Glashow-Iliopoulos-Maiani (GIM) mechanism [6]. It is therefore interesting to study the $\Lambda_b^0 \rightarrow \Lambda \mu^+ \mu^-$ decay and in particular its branching ratio $\mathcal{B}(\Lambda_b^0 \rightarrow \Lambda \mu^+ \mu^-)$. Charge conjugation is implied throughout this thesis. The $\mathcal{B}(\Lambda_b^0 \rightarrow \Lambda \mu^+ \mu^-)$ is measured using the $\mathcal{B}(\Lambda_b^0 \rightarrow J/\psi \Lambda)$ as a normalisation channel. Recent measurements from LHCb on $\mathcal{B}(\Lambda_b^0 \rightarrow \Lambda \mu^+ \mu^-)$ have shown slight tensions with the SM predictions [7]. These tensions contribute to a larger set of tensions known as the flavour anomalies [8, 9], which attract considerable attention from the particle physics community. Figure 3 shows the measured $\mathcal{B}(\Lambda_b^0 \rightarrow \Lambda \mu^+ \mu^-)$ in bins of the dilepton mass squared (q^2) where the shown SM prediction calculations are taken from [10]. The empty q^2 regions are the charmonium resonances of J/ψ and $\psi(2S)$ which are not $b \rightarrow s$ transitions and are therefore not relevant for this measurement. The measurements are consistent with the predictions in the low- q^2 region, but there is a pattern of inconsistencies in the high- q^2 region. The uncertainties on the $\mathcal{B}(\Lambda_b^0 \rightarrow \Lambda \mu^+ \mu^-)$ are dominated by the normalisation channel uncertainties. As such, a more precise measurement of the branching fraction $\mathcal{B}(\Lambda_b^0 \rightarrow J/\psi \Lambda)$ is needed to increase the precision of $\mathcal{B}(\Lambda_b^0 \rightarrow \Lambda \mu^+ \mu^-)$.

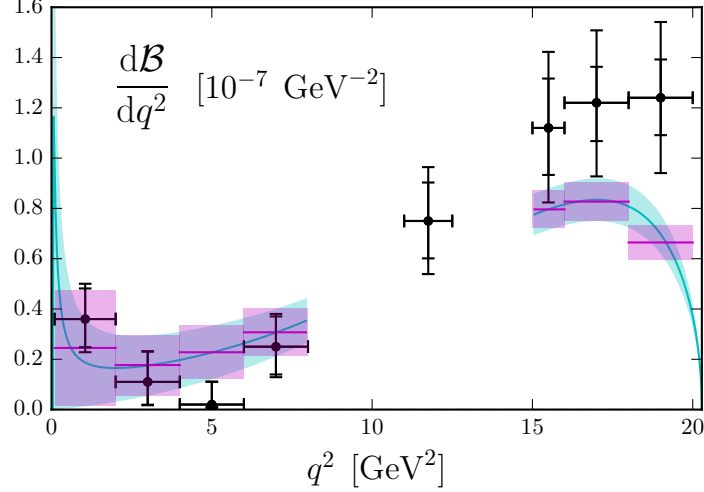


Figure 3: Measured $\mathcal{B}(\Lambda_b^0 \rightarrow \Lambda \mu^+ \mu^-)$ in bins of q^2 compared to SM predictions. The outer error bars include the uncertainties from the normalisation channel $\Lambda_b^0 \rightarrow J/\psi \Lambda$. Figure taken from [10]

The $\mathcal{B}(\Lambda_b^0 \rightarrow J/\psi \Lambda)$ is also needed as normalisation channel in the analysis searching for the charged Lepton Flavour Violating (LFV) decay $\Lambda_b^0 \rightarrow \Lambda e^\pm \mu^\mp$. In the SM, lepton flavour is conserved due to a missing neutrino mass term in the Yukawa lagrangian. With the discovery of neutrino oscillations, which implies that neutrinos have nonzero mass, it became clear that lepton flavour is not perfectly conserved. Therefore, searches for LFV have become more interesting and in particular, searches of LFV in baryon decays has not been investigated as extensively as for meson decays. The $\Lambda_b^0 \rightarrow \Lambda e^\pm \mu^\mp$ decay is a perfect candidate for LFV searches in the baryon sector due to the abundance of produced Λ_b^0 and the clean signature in the detector. Alternative models, where the interaction is mediated by new particles such as leptoquarks, predict a detectable value of the branching ratio of $\Lambda_b^0 \rightarrow \Lambda e^\pm \mu^\mp$ [11].

The branching ratio $\mathcal{B}(\Lambda_b^0 \rightarrow J/\psi \Lambda)$ has not yet been measured at the LHC. The most recent measurement has been performed in 2011 in the D0 experiment at the Tevatron Collider of Fermilab [12]. This measurement has large uncertainties, primarily due to lack of knowledge on the Λ_b^0 production. The data recorded at LHCb during the four years of Run 2 provide enough statistics to perform a new measurement of the $\Lambda_b^0 \rightarrow J/\psi \Lambda$ branching ratio with lowest uncertainties to date. This measurement will be used to reduce uncertainties in the $\Lambda_b^0 \rightarrow \Lambda \mu^+ \mu^-$ and $\Lambda_b^0 \rightarrow \Lambda e^\pm \mu^\pm$ branching ratio measurements as well as in any other analysis that will use $\Lambda_b^0 \rightarrow J/\psi \Lambda$ as a normalization channel, such as analyses of other b-baryon decays. In this analysis, the measurement of $\mathcal{B}(\Lambda_b^0 \rightarrow J/\psi \Lambda)$ is performed with $B^0 \rightarrow J/\psi K_S^0$ as a normalisation channel. The tree level Feynman diagrams of the $\Lambda_b^0 \rightarrow J/\psi \Lambda$ and $B^0 \rightarrow J/\psi K_S^0$ decays are shown in Figures 4 and 5, respectively. The diagrams show the quark content of all particles involved in the decays. Both decays are rare charged current $b \rightarrow c$ transitions. The strategy of the analysis is discussed in the following section.

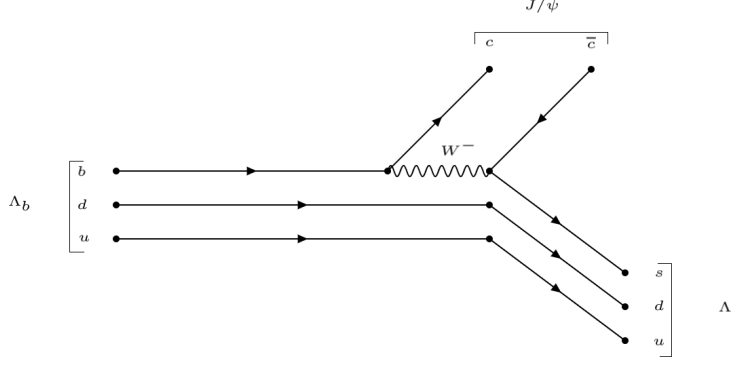


Figure 4: Tree level $\Lambda_b^0 \rightarrow J/\psi \Lambda$ Feynman diagram

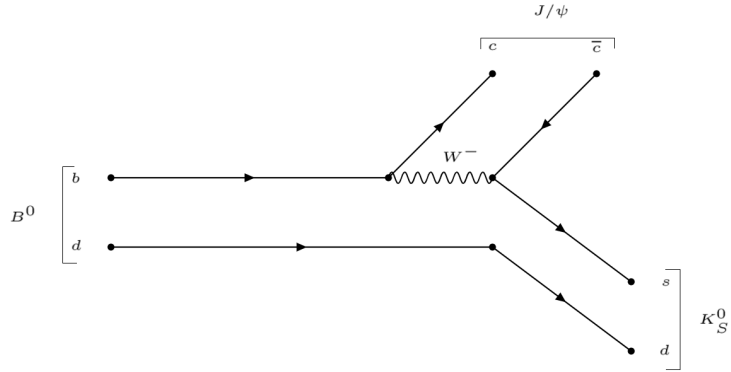


Figure 5: Tree level $B^0 \rightarrow J/\psi K_S^0$ Feynman diagram

1.2 Analysis Strategy

The goal of this analysis is to measure $\mathcal{B}(\Lambda_b^0 \rightarrow J/\psi \Lambda)$ using the full Run 2 data taken at LHCb at centre-of-mass energy of $\sqrt{s} = 13$ TeV. The integrated recorded luminosity in each of the years of Run 2 is shown in Table 1. The total luminosity collected during the whole Run 2 amounts to approximately 6 fb^{-1} of pp collisions. The addition of Run 1 data could potentially reduce the statistical uncertainty by 10%, but this comes at the cost of extra uncertainties due to different (and changing) trigger conditions. Furthermore, the final uncertainty on this branching ratio measurement will be limited by the systematic uncertainties, and not by the size of the data sample, and therefore it is decided to not include the Run 1 data sample.

Year	2015	2016	2017	2018
Integrated luminosity $\int \mathcal{L}(\text{fb}^{-1})$	0.33	1.67	1.71	2.19

Table 1: Integrated luminosity recorded at the LHCb experiment in Run 2 by year [13]

The analysis strategy is to measure $\mathcal{B}(\Lambda_b^0 \rightarrow J/\psi \Lambda)$ using $B^0 \rightarrow J/\psi K_S^0$ as a normalisation channel. The B^0 normalisation channel is used since there is no absolute measurement

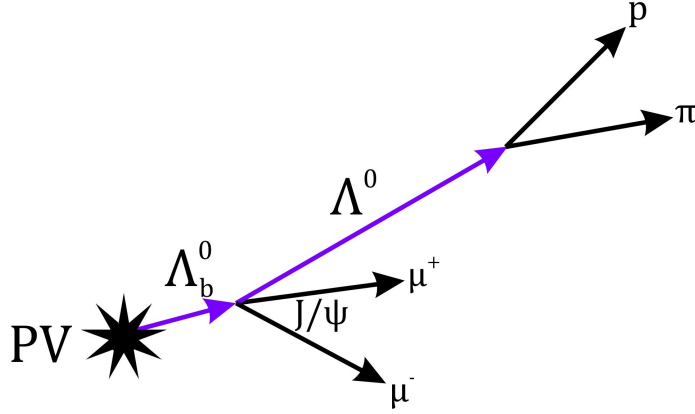


Figure 6: Topology of the $\Lambda_b^0 \rightarrow J/\psi \Lambda$ decay

of a Λ_b^0 branching fraction. The B^0 decay is chosen as a normalisation channel due to the topological similarity with $\Lambda_b^0 \rightarrow J/\psi \Lambda$. A schematic view of the $\Lambda_b^0 \rightarrow J/\psi \Lambda$ decay is shown in Figure 6. The b-hadron Λ_b^0 (B^0) travels about 10 mm before it decays to a J/ψ meson and a Λ baryon (K_S^0 meson). The J/ψ has a very small lifetime hence it decays practically instantly, while the Λ/K_S^0 travels a longer distance of about 1m before decaying, due to a longer lifetime. The J/ψ candidates are reconstructed as $\mu^+\mu^-$ final states while Λ and K_S^0 are reconstructed as $p\pi^-$ and $\pi^+\pi^-$ final states, respectively. The analysis strategy is described by the following equation:

$$\mathcal{B}(\Lambda_b^0 \rightarrow J/\psi \Lambda) = \mathcal{B}(B^0 \rightarrow J/\psi K_S^0) \times \frac{f_d}{f_{\Lambda_b^0}} \times \frac{N_{\Lambda_b^0}}{N_{B^0}} \times \frac{\varepsilon_{B^0}}{\varepsilon_{\Lambda_b^0}} \times \frac{\mathcal{B}(K_S^0 \rightarrow \pi^+\pi^-)}{\mathcal{B}(\Lambda \rightarrow p\pi^-)} \quad (1)$$

In Equation 1, $\mathcal{B}(B^0 \rightarrow J/\psi K_S^0)$ is the branching ratio of the $B^0 \rightarrow J/\psi K_S^0$ decay mode, while $\mathcal{B}(K_S^0 \rightarrow \pi^+\pi^-)$ and $\mathcal{B}(\Lambda \rightarrow p\pi^-)$ are the branching ratios of the K_S^0 to two pions and of the Λ to a proton and a pion. The most recent measurements of these branching ratios are given in the 2020 edition of the Particle Data Group (PDG) [14]. In particular, the PDG does not directly report $\mathcal{B}(B^0 \rightarrow J/\psi K_S^0)$, instead $\mathcal{B}(B^0 \rightarrow J/\psi K^0) = (8.67 \pm 0.30) \times 10^{-4}$ is reported. In this thesis, the K^0 is assumed to decay equally as K_S^0 and K_L^0 such that the branching ratio of $B^0 \rightarrow J/\psi K_S^0$ is taken to be 50% of the $B^0 \rightarrow J/\psi K^0$ branching ratio. $N_{\Lambda_b^0}$ and N_{B^0} are the Λ_b^0 and B^0 signal yields, while $\varepsilon_{\Lambda_b^0}$ and ε_{B^0} are the signal efficiencies of the selections performed in the Λ_b^0 and B^0 channels, respectively. Finally, since the normalization channel is a B^0 rather than a Λ_b^0 channel, the $f_{\Lambda_b^0}/f_d$ term accounts for the relative production between Λ_b^0 and B^0 . At LHCb, the measurement on b-hadron production in Run 2 [15] reported a dependence of the production fraction $f_{\Lambda_b^0}/f_d$ on the $p_T(\Lambda_b^0)$, as it can be seen in Figure 7 (left). The p_T dependence has only been measured in the fiducial range $4 < p_T(\Lambda_b^0) < 25 \text{ GeV}/c$ and it is described by an exponential function. There was no η dependence observed for the production fraction, as shown in Figure 7 (right). Thus, on top of the regular selection, an additional selection on the $p_T(\Lambda_b^0)$ and on the pseudorapidity η due to the LHCb detector geometrical acceptance ($2 < \eta < 5$)

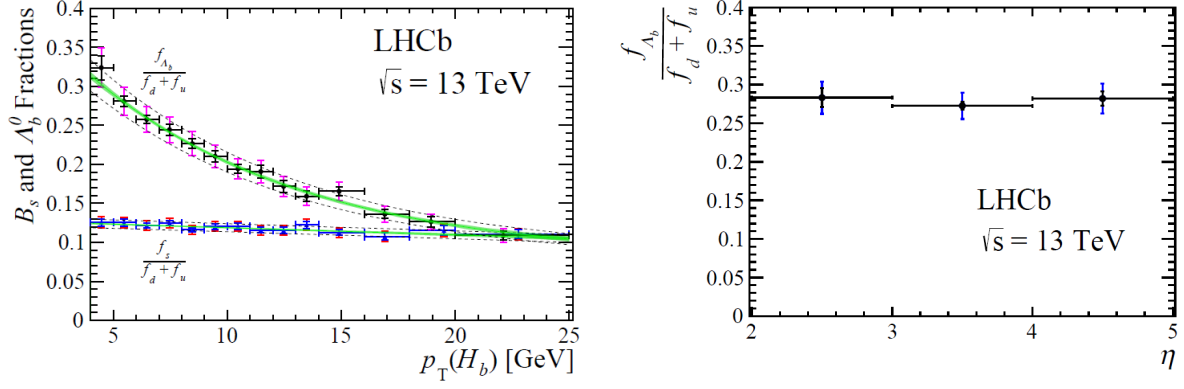


Figure 7: Dependence of the production fraction $f_{\Lambda_b^0}/f_d$ on $p_T(\Lambda_b^0)$ (left) and $\eta(\Lambda_b^0)$ (right). Figures taken from Ref. [15]

has to be performed. In this thesis the average value of $f_{\Lambda_b^0}/f_d$ is used in the computation of $\mathcal{B}(\Lambda_b^0 \rightarrow J/\psi \Lambda)$.

In chapter 2 of the thesis, an overview of the LHCb detector is given. Chapter 3 gives an overview of the selection steps performed on both decays where selections are kept as similar as possible. The fit model and the Λ_b^0 and B^0 signal yields are extracted and described in Chapter 4. The efficiencies together with Monte Carlo corrections are presented in Chapter 5. However, the corrections are not applied to generator level in order to obtain the corrected efficiencies. In Chapter 6, the final result is calculated using Equation 1 and discussed. Finally, conclusions and outlook for further research are presented in Chapter 7.

2 The LHCb detector at the Large Hadron Collider

2.1 LHC

The Large Hadron Collider (LHC) [16] is the largest particle accelerator and collider ever built, with a circumference of approximately 27 km. It is located about 100 m underground near Geneva, Switzerland and it is operated by the European Organization for Nuclear Research (CERN). It consists of a circular tunnel where bunches of protons are accelerated in opposite directions and collided at a centre of mass energy $\sqrt{s} = 13$ TeV in Run 2 [17]. The proton bunches cross at four collision points, where detectors are placed to record and study the particles produced in the collisions. The four main experiments located at these four collision points are: ATLAS (A Toroidal LHC Apparatus), CMS (Compact Muon Solenoid), ALICE (A Large Ion Collider Experiment) and LHCb (Large Hadron Collider beauty). ATLAS and CMS are the largest detectors at the LHC and are general-purpose detectors, designed to study a wide range of physics [18, 19]. ALICE and LHCb are the two smaller detectors designed to study more specific physics processes. ALICE is a heavy-ion detector which studies strong interaction processes (QCD) by studying the quark gluon plasma, an extreme state of matter produced in heavy nuclei (Pb-Pb) collisions [20]. The LHCb experiment is dedicated to studying flavour physics and CP violation by studying the interactions of b- and c-hadrons [21].

2.2 The LHCb detector

The LHCb detector is one of the four main experiments at CERN and its main purpose is to study and measure rare decays of b- and c-hadrons and the CP violation parameters these decays give access to.

At the high centre-of-mass energy the LHC is operated at, proton-proton collisions produce $b\bar{b}$ quark pairs at small angles with respect to the beam axis, in forward or backward directions. The LHCb detector takes advantage of this by having a forward geometry. The LHCb coordinate system can be seen in Figure 8, where z is the axis along the beam, y is perpendicular to it in the plane of the figure and x is perpendicular to the plane of the figure. Instead, the z , ϕ and θ coordinate system can be used, where ϕ is the angle between the x and y axes and θ is the angle between z and y . The pseudorapidity η is a Lorentz invariant quantity which is often used instead of the angle θ to express angular coverage, and it is defined as:

$$\eta = -\ln(\tan(\theta/2)) \quad (2)$$

The LHCb has a very forward geometric acceptance of $2 < \eta < 5$ which is equivalent to about 15-250 mrad.

As can be seen from the detector cross-section in Figure 8, LHCb consists of several subdetectors which are all essential to detect, measure properties of and identify the particles produced in the pp collisions. The LHCb subdetectors can be categorized as: tracking system, calorimeter system, RICH detectors and muon system.

The tracking system at LHCb consists of the VERtex LOCator (VELO) and four tracking stations: the Tracker Turicensis (TT) stations before the magnet and the T1, T2, T3 stations after the magnet. The VELO [22] is a silicon strip detector placed very close to the interaction point, at a distance of only 8 mm. After b-hadrons are produced at the

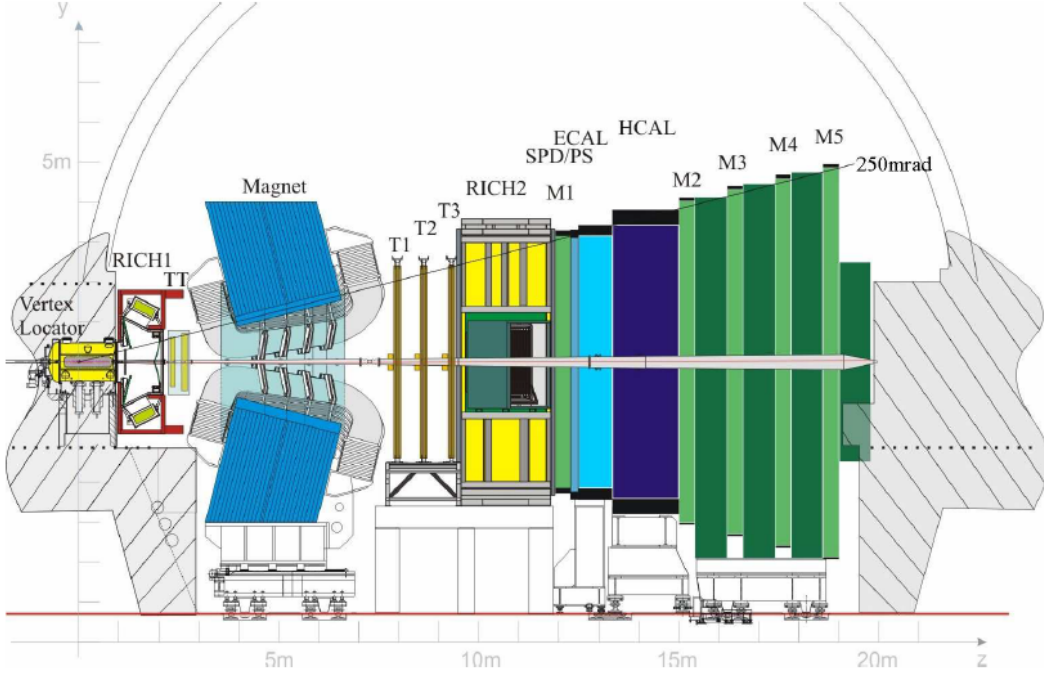


Figure 8: Schematic view of the LHCb detector [21]

pp primary vertex (PV), they travel about 1 cm before they decay at a displaced secondary vertex (SV), due to their short lifetimes. The VELO is able to very precisely measure tracks close to the interaction point and distinguish between primary and secondary vertices such that b-hadrons coming from displaced vertices can be reconstructed and their lifetimes can be accurately measured. The resolution of the vertex location measurement is heavily dependent on the number of tracks in the vertex, i.e. it improves with track multiplicity [23]. The T1, T2 and T3 stations consist of the Inner Tracker (IT) which is closer to the beam pipe covering the high η acceptance, and the Outer Tracker (OT) which covers the rest of the η acceptance. The TT stations and the IT are made of silicon strips and together form the Silicon Trackers (ST) [24]. The ST cover the region close to the pipe, i.e. high η region, where the particle flux is very high hence silicon detectors with better spatial resolution have been chosen. In the OT, gas drift tubes, also called straw tubes, are used to track charged particles in the lower η regions [25]. With this configuration of the tracking system, the b-hadron is produced and decays inside the VELO, which measures the location of its decay vertex, while the daughter particle tracks are measured either by the VELO or by the other tracking stations, depending on their lifetime. A magnet is used to bend the trajectories of charged particles thus allowing for a measurement of their momenta by measuring the curvature of the tracks. The bending power of the magnet is $\int Bdl = 4 \text{ Tm}$ for 10m long tracks [26]. The TT stations are placed before the magnet in order to measure tracks of particles with low momenta whose trajectories would be significantly curved by the bending of the magnet and would otherwise go out of the detector acceptance. The polarity of the magnet is switched periodically in order to cancel the effect of systematic uncertainties arising from detection asymmetries. Therefore, the recorded data is split in *MagUp* and *MagDown*

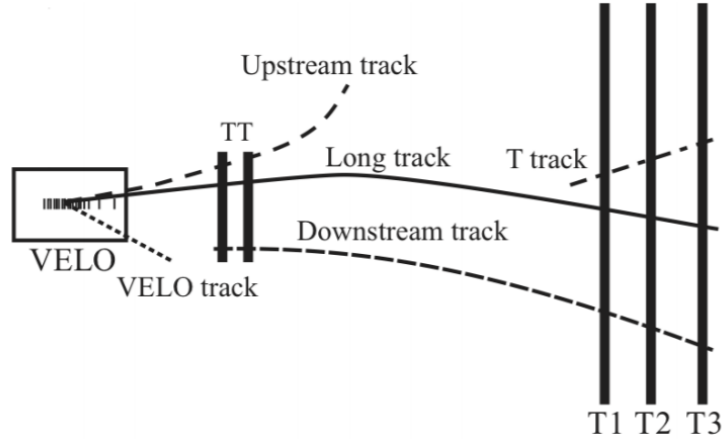


Figure 9: Overview of track types at LHCb [27]

samples. In this analysis, the two data samples are combined. The tracking system has a momentum measurement resolution from 0.4% at 5 GeV/ c to 1% at 200 GeV/ c [23]. Additionally, LHCb achieves a good resolution on the track impact parameter (IP), i.e. the minimum distance of the track to the PV. This is important because the daughter particles of the b -hadrons have large p_T and therefore large IP values. Selections on the IP help distinguish b -hadron decays from background decays.

Finally, it is useful to define the different track categories at LHCb. The tracks are defined based on where the hits are recorded within the LHCb detector. As such, tracks with hits only in the VELO are called VELO tracks, while tracks with hits in both VELO and the TT stations are named upstream tracks. A track that has hits in all the tracking subdetectors, i.e. in VELO, TT and T stations is called a long track. Due to having a longer lifetime, Λ and K_S^0 particles often decay after the VELO, leaving hits only in the TT and T stations. A track reconstructed from hits in these stations is called a downstream track and is the only track category that is used in this analysis of Λ and K_S^0 decays. Finally, a track with hits only in the T stations is called a T track. An overview of the track categories is shown in Figure 9.

The calorimeter system of LHCb [28] consists of the Scintillating Pad Detector (SPD), the Pre-Shower Detector (PS), the Electromagnetic Calorimeter (ECAL) and the Hadronic Calorimeter (HCAL). There is a thin layer of lead between the SPD and the PS. The SPD mainly distinguishes between electrons and photons or neutral pions, as electrons produce scintillations in the SPD while the photons interacting with the lead layer produce electromagnetic showers detected by the PS. The ECAL measures the energy deposition of particles that interact via the electromagnetic interaction such as electrons and photons, while the HCAL measures the energy deposition of neutral and charged hadrons. The ECAL is composed of layers of scintillating material and lead, while the HCAL is composed of alternating layers of scintillator and iron. Besides the energy measurement, the HCAL also provides the L0 trigger information about high transverse energy (E_T) hadrons [21]. The trigger system is described in Section 3.1.

The two Ring Imaging CHerenkov (RICH) detectors [29] are responsible for the particle identification (PID) at the LHCb experiment. The detection principle is based on the

Cherenkov radiation emitted by a charged particle travelling in a medium faster than the speed of light in that medium. The Cherenkov light is emitted at an angle with respect to the particle trajectory, which is directly related to the speed of the particle and the refractive index of the medium. The RICH detectors are made of a radiator volume and a set of mirrors that reflect the Cherenkov light to an array of photomultiplier tubes (PMTs). The RICH1 detector has two radiators, silica aerogel and C_4F_{10} which cover particle momentum ranges up to 40 GeV/ c , and it is positioned before the magnet to cover a larger angle. The RICH2 detector is positioned after the magnet and it consists of a CF_4 radiator. It operates in a particle momentum range of up to 100 GeV/ c .

The muon system [30] consists of five plane stations (M1-M5) which are used to identify and measure the tracks of muons. The detector technology used in the muon system consists of Multi Wire Proportional Chambers (MWPC). These are gas detectors where the charge created by a passing ionizing particle is collected by the anode wire. The muon stations are placed at the end of the detector, farthest away from the interaction point, since muons are the only particles that can penetrate all other subdetectors and reach the stations. The M2-M5 muon stations are separated by 80 cm layers of iron to ensure that any other particles will not traverse all muon stations. The muon event is sent to the L0 trigger only if it passed all 5 stations, making the muon system highly efficient in muon identification. The M1 station is placed in front of the calorimeters in order to increase the resolution on the p_T measurement. Due to the high particle rate in this region, M1 uses Gas Electron Multiplier (GEM) detector instead of MWPC.

3 Data flow and event selection in Run 2

In this chapter, an overview is given of the various steps of the data processing at the LHCb detector. At each step the data is filtered such that only a fragment is saved at the end for analysis purposes.

At the LHC, proton-proton bunch-crossings take place at a rate of up to 40 MHz which, in terms of storage, would amount up to 1 TB/s, which is far too much to record [31, 32]. For this reason, there are multiple selection steps that reduce the number of events to a manageable amount. The first selection step is the trigger, which consists of a hardware and a software level. The trigger system has the purpose to decide which events are saved and selects them already during data-taking, reducing the rate to 1 MHz after the hardware level and further down to 12.5 kHz after the software level. The trigger system is described in more detail in Section 3.1. After the trigger, raw data is reconstructed offline into objects such as tracks and clusters based on the hits in the tracking detectors and in the calorimeters. The calorimeter clusters as well as information from RICH detectors is used for particle identification (PID). The second selection step is the stripping, where particle candidates are constructed using the objects obtained in reconstruction and loose cuts based on kinematic and geometric properties of the particles are applied. Stripping is discussed in Section 3.2. Finally, an offline selection that is designed for the analysis is performed which is discussed in Section 3.3.

3.1 Trigger selection

The first step of data selection is the trigger [31, 32]. There is a hardware (Level 0 or L0) trigger and a software (High Level Trigger or HLT) trigger. The HLT consists of two levels: the HLT1 and HLT2 triggers. The purpose of the trigger system is to reduce the 40 MHz rate to a rate that can be saved on disk while remaining highly efficient for signal. Therefore, the trigger reduces the rate by three orders of magnitude down to $\mathcal{O}(10)$ kHz [33].

The hardware L0 trigger reduces the 40 MHz event rate to 1 MHz. This is done based on the information from muon stations and calorimeters only. Since the decay products of b- and c- hadrons typically have a large transverse momentum relative to particles from pp collisions (due to their large mass), the L0 trigger selects events with a large transverse energy E_T deposited in the calorimeters or high p_T muon tracks. The thresholds for both the hadron and the muon triggers vary with the different years of Run 2 but are all in the order of a few GeV [34]. In addition, there is a di-muon L0 trigger which requires the largest of the two muon p_T to be above the L0Muon threshold or the product of two muons p_T to be above the L0DiMuon threshold. In this analysis, both L0Muon and L0DiMuon trigger lines are used.

All events that pass L0, i.e. the 1 MHz output, move on to the HLT1 trigger. In HLT1, a minimal reconstruction of the events is performed. Information from the VELO is used to reconstruct tracks, extending them to the TT (upstream tracks) stations and eventually to the T stations (long tracks), or to the muon stations if the event was triggered by L0Muon. The reconstruction of the primary vertex also takes place at the HLT1 level and is based only on the VELO tracks. Afterwards, events are filtered by applying selections to the track χ^2 , impact parameter with respect to a primary vertex (displacement from the PV) and p_T . This analysis uses HLT1 trigger lines that require muon identification as

L0	JPs_L0MuonDecision_TOS
	JPs_L0DiMuonDecision_TOS
HLT1	JPs_Hlt1TrackMuonMVADecision_TOS
	JPs_Hlt1TrackMVADecision_TOS
	JPs_Hlt1TrackMuonDecision_TOS
	JPs_Hlt1DiMuonHighMassDecision_TOS
HLT2	Lb_Hlt2Topo2BodyDecision_TOS
	Lb_Hlt2Topo3BodyDecision_TOS
	Lb_Hlt2TopoMu2BodyDecision_TOS
	Lb_Hlt2TopoMu3BodyDecision_TOS
	Lb_Hlt2TopoMuMu2BodyDecision_TOS
	Lb_Hlt2TopoMuMu3BodyDecision_TOS
	Lb_Hlt2DiMuonDetachedJpsiDecision_TOS

Table 2: Trigger lines used in this analysis

well as lines that do not. In addition, the `DiMuonHighMass` line is used to trigger events with two muon tracks which are displaced from the PV and have an invariant mass larger than the set threshold.

At the HLT2 level, the same event reconstruction as done offline takes place for both charged and neutral particles. In addition to muon identification which was already available in HLT1, the full PID information from the RICH systems and calorimeters is used. Due to lower thresholds, HLT2 is able to trigger tracks with lower p_T that were not previously triggered. In addition, tracks of particles that decay outside the VELO due to their large lifetime, such as Λ or K_S^0 , are reconstructed as downstream tracks using the hits in the T and TT stations. HLT2 selects events based on track χ^2 , p_T and PID. An event rate of 12.5 kHz passes the HLT2 trigger and is then saved to disk. The HLT2 lines used in this analysis are called topological trigger lines. These lines trigger events with two, three or four charged tracks forming a vertex that is significantly displaced from the PV and with a topology compatible with a b-hadron decay [34]. HLT2 lines with and without requiring the presence of a muon are used. In addition, the `DiMuonDetached` line is used to trigger di-muon tracks detached from the PV.

An overview of the L0, HLT1 and HLT2 trigger lines used is given in Table 2. In this analysis, all candidates are Trigger on Signal (TOS) which means the daughter particles of the J/ψ and Λ candidates have to be responsible for triggering the b-hadron event.

3.2 Stripping selection

The second step in event selection is stripping, which is done offline after the trigger. Due to the large data volumes and large CPU requirements this stripping selection step is run centrally by the collaboration. At this step, the $\Lambda_b^0 \rightarrow J/\psi \Lambda$ decay is fully reconstructed using the final state particle tracks. The Λ candidate is constructed from a $p\pi$ pair, while the J/ψ is constructed from a $\mu^+\mu^-$ pair. Finally, the Λ and J/ψ candidates are combined to form the Λ_b^0 candidate. After the reconstruction, a set of loose kinematic and geometric cuts are applied to reduce the data to a manageable amount for analysis. An overview of

the stripping selection is given in Table 3.

The two muons that form the J/ψ need to pass **IsMuon**, i.e to have hits that are consistent with a muon hit. **IsMuon** is a binary variable that performs a loose identification of muons based on their penetration in the calorimeters and iron filters [35]. The muons need to be detached from a PV by requiring a χ_{IP}^2 with respect to the PV larger than 9. The p_{T} of each muon is required to be larger than 350 MeV/ c . The invariant mass of the two muons has to be less than 5500 MeV/ c^2 and the p_{T} larger than 0 MeV/ c . The J/ψ candidate needs to have a good vertex $\chi_{\text{vtx}}^2 < 9$, a flight distance $\chi_{\text{FD}}^2 > 16$ and a χ_{IP}^2 with respect to a PV larger than 0. The proton and the pion that form the Λ candidate need to have a total momentum larger than 2 GeV/ c and an $\chi_{\text{IP}}^2 > 4$ with respect to the PV for both the proton and the pion. The Λ candidate is required to have a good vertex $\chi_{\text{vtx}}^2 < 9$ and a p_{T} larger than 400 MeV/ c . Additionally, its invariant mass is required to be in a 64 MeV/ c^2 window around the PDG value [14]. Finally, the Λ_b^0 candidate must have an invariant mass of 5500 MeV/ c^2 around the PDG value, a good vertex $\chi_{\text{vtx}}^2 < 27$, a $\chi_{\text{FD}}^2 > 100$ and a cosine of the angle between the momentum of the particle and the direction of flight from the best PV to the decay vertex, DIRA, close to 1. In addition, the Λ_b^0 candidate is required to have an $\chi_{\text{IP}}^2 < 25$. As opposed to the other particles which need to have significant displacement from the PV, i.e. a large χ_{IP}^2 , the Λ_b^0 particle does actually decay very close to the PV so the χ_{IP}^2 needs to be small. As shown in Chapter 2, Λ candidates can be reconstructed from long or downstream tracks. In this analysis only down-down (DD) $p\pi$ tracks are used.

The stripping line used in this analysis is **StrippingBu2LLK_mmLine**¹ which is used for decays of b-hadrons (B^+ , B^- , B^0 , Λ_b^0) to a di-lepton pair and a hadron. After the stripping, the remaining events are saved into so-called nTuples which is the data format used during analysis.

3.3 Offline selection/Preselection

As described in Chapter 1, this analysis measures the branching ratio of $\Lambda_b^0 \rightarrow J/\psi \Lambda$ with the decay $B^0 \rightarrow J/\psi K_S^0$ as normalisation channel since the two decays are very similar in kinematics. Therefore, the selection for the two decays is kept as identical as possible with the exception of the Λ/K_S^0 mass selection, as discussed later in this section.

The purpose of the offline selection is to remove candidates that can not be good signal candidates. The signal efficiency of the selections is checked using Monte-Carlo (MC) samples. The offline selection consists of a set of requirements which are tighter than the ones in stripping as they are more optimised for this analysis. An overview of the offline selection is given in Table 4. The fiducial Λ cuts aim to remove unphysical candidates, i.e. background, by keeping only Λ candidates that have a flight distance χ^2 larger than 0, a measured lifetime $\tau(\Lambda)$ between 0.5 and 2000 ps, a DIRA angle larger than 0 and a decay vertex z distance Z_{DV} smaller than 2250 mm. The $Z_{\text{DV}}(\Lambda) < 2250$ mm selection removes the excess of Λ candidates at $Z_{\text{DV}}(\Lambda) \approx 2300$ mm. These are not real candidates, but come from a background effect of the Λ particle interacting with the detector material at the RICH1 interface. Figure 10a shows the distribution of the Λ endvertex z variable in 2018 data and MC with the selection criteria indicated by the red dotted lines. By comparing data with MC, it becomes clear that the preselection is mostly

¹Different stripping versions are used for the different Run 2 years, namely 24r2, 28r2, 29r2 and 34 for 2015, 2016, 2017 and 2018, respectively. The different versions can have small differences between them.

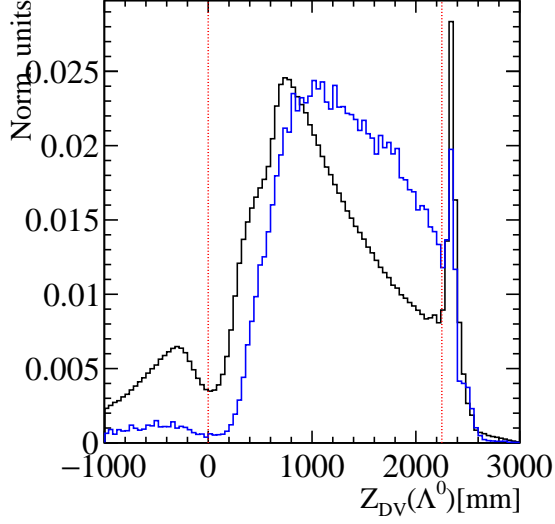
μ^\pm	
isMuon	TRUE
hasMuon	TRUE
p_T	$> 350 \text{ MeV}/c$
χ_{IP}^2	> 9
J/ψ	
m	$< 5500 \text{ MeV}/c^2$
χ_{vtx}^2	< 9
χ_{FD}^2	> 16
χ_{IP}^2	> 0
p_T	$> 0 \text{ MeV}/c$
Λ_b^0	
$ m - m_{\text{PDG}} $	$< 1500 \text{ MeV}/c^2$
χ_{vtx}^2	< 27
χ_{FD}^2	> 100
χ_{IP}^2	< 25
DIRA	> 0.9995
Λ	
p_T	$> 400 \text{ MeV}/c$
$ m - m_{\text{PDG}} $	$< 64 \text{ MeV}/c^2$
χ_{vtx}^2	< 25
p	
p	$> 2 \text{ GeV}/c$
χ_{IP}^2	> 4
π	
p	$> 2 \text{ GeV}/c$
χ_{IP}^2	> 4

Table 3: Overview of the Bu2LLK_mm stripping line requirements

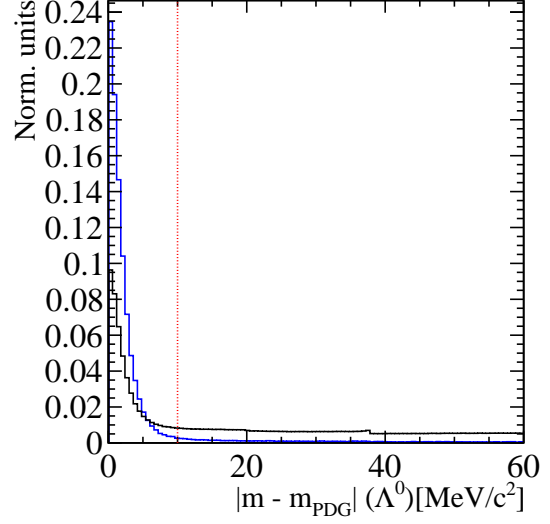
highly efficient on signal candidates. In this figure, data and MC are compared before any offline selection is applied, i.e. directly after stripping, such that the data distribution contains a lot of background. Figure 10b shows the cut on the Λ invariant mass where we see again that the cut removes the tail of the distribution which consists almost entirely of background. The distributions of all variables used in the offline selection along with the selection criteria are shown for 2018 data in Appendix A for both $\Lambda_b^0 \rightarrow J/\psi \Lambda$ and $B^0 \rightarrow J/\psi K_S^0$.

The acceptance cut on the $p_T(\Lambda_b^0)$ is needed since the production fraction $f_{\Lambda_b^0}/f_d$ is only known in this fiducial range as shown in Chapter 1. The requirement on $\eta(\Lambda_b^0)$ is due to the LHCb detector pseudorapidity acceptance. The distributions of the $p_T(\Lambda_b^0)$ and $\eta(\Lambda_b^0)$ in 2018 data and MC with lines that indicate the selection criteria are shown in Figure 10c and 10d. These two variables are not modelled correctly in MC and will be corrected for in order to get a better estimate of the signal efficiency. The reweighting of these variables is described in Chapter 5.

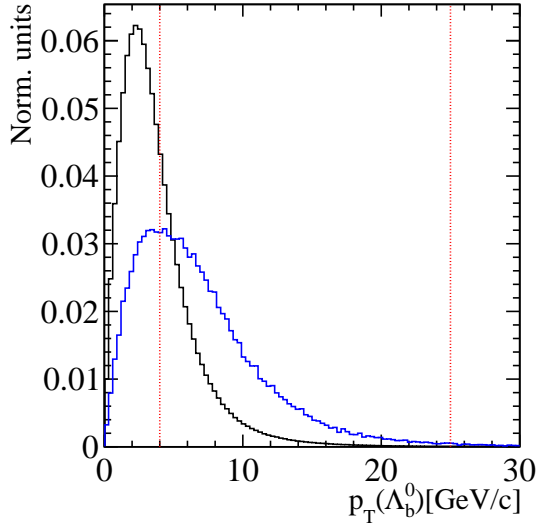
The Λ_b^0 mass cut helps remove combinatorial background in a region far away from the signal peak. In addition, the J/ψ and Λ masses are constrained to a 50 and 10 MeV/ c^2



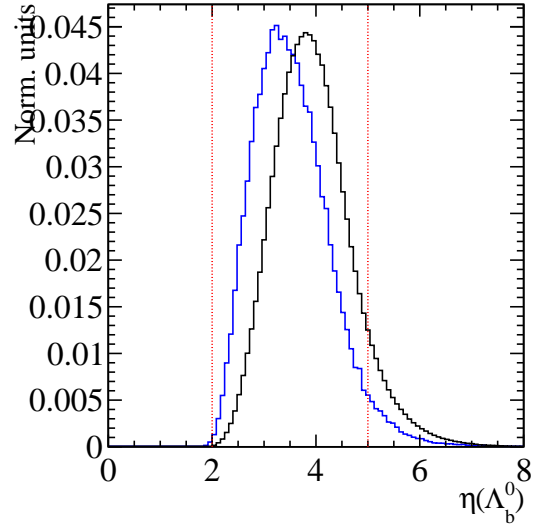
(a) Fiducial Λ decay vertex z cut



(b) Λ mass cut



(c) Acceptance Λ_b^0 p_T cut



(d) Acceptance Λ_b^0 pseudorapidity cut

Figure 10: Distributions of the Λ endvertex z (a) and mass cut (b). Also shown are the acceptance cuts on Λ_b^0 p_T (c) and η (d). 2018 data and MC are shown in black and blue, respectively. The dotted red line indicates the selection criteria. All plots are normalized.

μ^\pm	
p_T	$> 500 \text{ MeV}/c$
p	$> 3000 \text{ MeV}/c$
J/ψ	
$ m - m_{PDG} $	$< 50 \text{ MeV}/c^2$
$\Lambda (K_S^0)$	
χ_{FD}^2	> 0
Z_{DV}	$> 0 \text{ mm}$ $< 2250 \text{ mm}$
τ	$> 0.5 \text{ ps}$ $< 2 \text{ ns}$
DIRA	> 0
$ m - m_{PDG} $	$< 10 (15) \text{ MeV}/c^2$
Λ_b^0	
p_T	$> 4 \text{ GeV}/c$ $< 25 \text{ GeV}/c$
η	> 2 < 5
m	$> 4800 \text{ MeV}/c^2$

Table 4: Overview of preselection cuts. All cuts are identical for both Λ_b^0 and B^0 channels, except for the invariant mass of the two final state hadrons. The B^0 selection is indicated in the parenthesis

window around their PDG values. The only difference in selection between the Λ_b^0 and the B^0 channels is the mass cut on the K_S^0 which is 15 MeV/c^2 around its PDG mass value, instead of 10 MeV/c^2 . This is because the K_S^0 is lighter than the Λ and more momentum is released in its decay. The track momentum resolution increases with larger momentum so a 10 MeV/c^2 cut around the PDG value for the $\pi\pi$ invariant mass would be too tight such that a cut of 15 MeV/c^2 is chosen instead.

The muon p_T requirements are meant to select only events above the muon p_T and p thresholds of 500 and 3000 MeV/c^2 , respectively. This is needed for the calibration of Monte-Carlo samples in PID variables for which we need to make sure that the selection on data and MC is aligned.

4 Mass fit model and signal yield extraction

After the data passed all selection steps, the remaining data is used to determine the number of signal events, i.e. the signal yield. This is achieved by performing a fit ² on the invariant mass distribution of both $\Lambda_b^0 \rightarrow J/\psi \Lambda$ and $B^0 \rightarrow J/\psi K_S^0$ from which the signal yields are extracted, as they are needed to compute $\mathcal{B}(\Lambda_b^0 \rightarrow J/\psi \Lambda)$, as shown in Equation 1. Besides signal, the invariant mass fits contain several background components that need to be modelled. Similar fit models are implemented in both Λ_b^0 and B^0 invariant mass fits.

The two types of background components that we need to deal with in this analysis are:

- **Combinatorial background.** This type of background comes from random combinations of final state particles, i.e. $\mu\mu p\pi$ for Λ_b^0 or $\mu\mu\pi\pi$ for B^0 , whose invariant mass ends up in the region of the Λ_b^0 or B^0 invariant mass.
- **Peaking background.** There are two types of peaking background that we encounter in this analysis: misidentified (misID) background and peaking background coming from another decay with the same final state. The misID background stems from a misidentification of a final state hadron. In the $\Lambda_b^0 \rightarrow J/\psi(\rightarrow \mu^+\mu^-)\Lambda(\rightarrow p\pi^-)$, a pion can be misidentified as a proton such that a $B^0 \rightarrow \mu\mu\pi\pi$ event will be wrongly reconstructed in the Λ_b^0 mass hypothesis. These events form a peaking background shifted from the Λ_b^0 signal mass peak. Similarly, a proton can be misidentified as a pion in the reconstruction of the $B^0 \rightarrow J/\psi(\rightarrow \mu^+\mu^-)K_S^0(\rightarrow \pi^+\pi^-)$ decay, resulting in a Λ_b^0 misID peaking background in the B^0 mass fit. The effect of misID backgrounds is significant as there are no PID cuts performed for DD Λ/K_S^0 candidates. By performing PID cuts, additional uncertainties in the efficiency are introduced due to an inaccurate modelling of PID variables in the MC. Therefore, the more simple approach of modelling the misID backgrounds in the fit has been chosen.

The second type of peaking background appears only in the $B^0 \rightarrow J/\psi K_S^0$ fit and comes from the decay of a different b-hadron to the same final state, namely $B_s^0 \rightarrow J/\psi K_S^0$. The B_s^0 decay is suppressed with respect to the B^0 decay by more than one order of magnitude due to the presence of the V_{cd} instead of V_{cs} CKM matrix element in the process amplitude. The smaller production fraction of B_s^0 compared to B^0 suppresses this background effect by an extra factor 4. Therefore, the contribution of the B_s^0 background is small.

For both the $\Lambda_b^0 \rightarrow J/\psi \Lambda$ and $B^0 \rightarrow J/\psi K_S^0$ the Run 2 data fits are split in two samples: R2p1 which consists of the first part of Run 2, i.e. 2015 and 2016, and R2p2 which consists of the last two years, 2017 and 2018. The modelling of the signal peak as well as the peaking background components is done using Monte Carlo simulation samples. The combinatorial background shape is determined from the sidebands in the invariant mass distribution.

²In this analysis, the `ewp-rx` framework was used to perform the fits. This framework contains C++ scripts and can be used to handle nTuples, apply selections to data and MC and run fits. Inside the framework, the fitting is performed by the `RooFit` package by maximizing the log-likelihood function [36]. `RooFit` is a C++ library that works in the ROOT environment and is widely used to model data in b-hadron decay analyses [37]

As already mentioned, the signal event yield is determined by performing a fit on the Λ_b^0 and B^0 invariant mass distributions. The actual variable used for fitting is however not the regular invariant mass variable but the **DecayTreeFitter** (DTF) version of the mass variable [38]. The DTF algorithm provides better estimates for the track parameters of the final state particles by imposing hypothesis-driven mass constraints and vertex constraints. The DTF variable used to fit in both decay channels has constraints on the Λ/K_S^0 and J/ψ invariant mass to the known PDG values as well as primary vertex constraints, i.e. the Λ_b^0/B^0 candidate has to come from its best PV.

4.1 Signal shape

The shape used to model the signal peak in both Λ_b^0 and B^0 decays is the so-called Ipatia function [39] given by

$$H(x; \mu, \sigma, \lambda, \zeta, \beta, a_1, n_1, a_2, n_2) \propto \begin{cases} h(m, \mu, \sigma, \lambda, \zeta, \beta), & \text{if } \frac{m-\mu}{\sigma} > -a_1 \text{ or } \frac{m-\mu}{\sigma} < a_2 \\ \frac{h(m-a_1\sigma, \mu, \sigma, \lambda, \zeta, \beta)}{\left(1-m/\left(n_1 \frac{h(m-a_1\sigma, \mu, \sigma, \lambda, \zeta, \beta)}{h'(m-a_1\sigma, \mu, \sigma, \lambda, \zeta, \beta)} - a_1\sigma\right)\right)^{n_1}}, & \text{if } \frac{m-\mu}{\sigma} \leq -a_1 \\ \frac{h(m-a_2\sigma, \mu, \sigma, \lambda, \zeta, \beta)}{\left(1-m/\left(n_2 \frac{h(m-a_2\sigma, \mu, \sigma, \lambda, \zeta, \beta)}{h'(m-a_2\sigma, \mu, \sigma, \lambda, \zeta, \beta)} - a_2\sigma\right)\right)^{n_2}}, & \text{if } \frac{m-\mu}{\sigma} \geq a_2 \end{cases} \quad (3)$$

with

$$h(m; \mu, \sigma, \lambda, \zeta, \beta) \propto ((m - \mu)^2 + A_\lambda^2(\zeta)\sigma^2)^{\frac{1}{2}\lambda - \frac{1}{4}} e^{\beta(m-\mu)} K_{\lambda-\frac{1}{2}} \left(\zeta \sqrt{1 + \left(\frac{m - \mu}{A_\lambda(\zeta)\sigma} \right)^2} \right). \quad (4)$$

In equation 3, $h(m; \mu, \sigma, \lambda, \zeta, \beta)$ is the hyperbolic core of the Ipatia function while $h'(m; \mu, \sigma, \lambda, \zeta, \beta)$ is its derivative with respect to m . In equation 4, $K_{\lambda-\frac{1}{2}}$ are special Bessel functions of the third kind and A_λ is a parametrization of the Bessel functions. The parameters $\mu, \sigma, \lambda, \zeta$ and β control the resolution of the hyperbolic core and a_1, n_1, a_2, n_2 are the parameters related to the tails of the distribution. During the fit of the signal peak shape to MC, only parameters ζ and β are kept constant, while all the others are left floating.

Both signal peaks are first fitted in a Monte-Carlo sample to determine the shape, i.e. fix the values of all parameters of the Ipatia function, except μ and σ . Afterwards, this shape is used in the final fit on data with μ and σ left floating. As an example, the $\Lambda_b^0 \rightarrow J/\psi \Lambda$ signal peak fitted with an Ipatia function in R2p2 MC is shown in Figure 11a and 11b in linear and logarithmic scale, respectively. It is visible that the Ipatia shape describes very well the signal peak and the pulls distribution is good. In addition, the Λ and J/ψ mass constraints of the DTF variable used for fitting are explicitly written in the mass variable name. The remaining signal shape fits for Λ_b^0 and B^0 in both R2p1 and R2p2 are given in Appendix B.

The parameters of the signal fit to MC for $B^0 \rightarrow J/\psi K_S^0$ are reported in Table 6 for both R2p1 and R2p2. All parameters are floating except ζ and β which are fixed at 0.005 and 0, respectively.

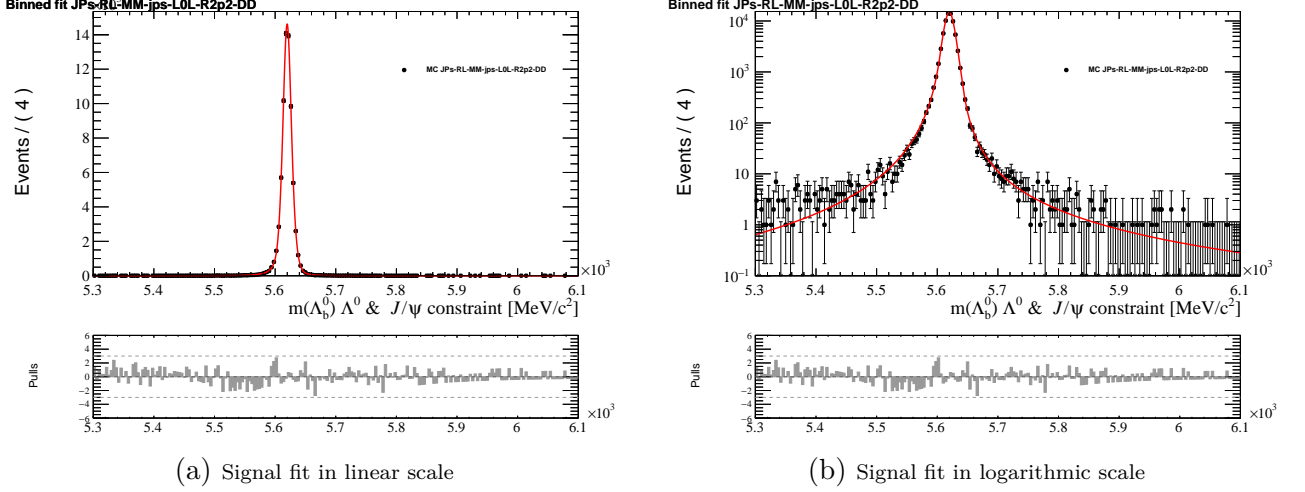


Figure 11: Signal shape fitted with Ipatia function for $\Lambda_b^0 \rightarrow J/\psi \Lambda$ in linear and log scale for the MC of R2p2

Floating parameter	Fit value	
	R2p1	R2p2
a_1	1.9805 ± 0.0470	1.7623 ± 0.0290
a_2	3.2870 ± 0.1156	2.7196 ± 0.0826
n_1	2.2532 ± 0.0758	2.4998 ± 0.0580
n_2	1.5177 ± 0.0897	1.8838 ± 0.0758
λ	-2.3941 ± 0.0963	-2.8494 ± 0.1377
μ	5619.7229 ± 0.0429	5619.8116 ± 0.0324
σ	9.4443 ± 0.1007	9.0195 ± 0.0896
Constant parameter		
ζ	0.005	0.005
β	0	0

Table 5: Parameters of Ipatia signal fit to MC for $\Lambda_b^0 \rightarrow J/\psi \Lambda$

Similarly, the $\Lambda_b^0 \rightarrow J/\psi \Lambda$ signal peak is first fitted using MC and the Ipatia function parameters are reported in Table 5. The ζ and β parameters are kept constant while all the other parameters are floating.

4.2 Modelling of peaking backgrounds

The shapes of the misidentified Λ_b^0 and B^0 backgrounds (in the $B^0 \rightarrow J/\psi K_S^0$ and $\Lambda_b^0 \rightarrow J/\psi \Lambda$ mass fits, respectively) are determined using Monte-Carlo templates. For the misID background template in the Λ_b^0 mass fit, $B^0 \rightarrow J/\psi K_S^0$ events are generated and reconstructed as Λ_b^0 by misidentifying the pion as a proton, and viceversa. The shape of the misID background for both mass fits is fitted with a `RooKeysPDF`, which consists of a superposition of Gaussian kernels. The width of each Gaussian is calculated from the local density of events [40]. The `RooKeysPDF` has only one parameter, ρ , which determines the smoothness of the curve. For all the fits presented in this thesis, the value

Floating parameter	Fit value	
	R2p1	R2p2
a_1	1.4629 ± 0.0127	1.4689 ± 0.0228
a_2	3.3059 ± 0.0399	3.347 ± 0.0755
n_1	3.3894 ± 0.0495	3.4267 ± 0.09
n_2	1.5021 ± 0.0284	1.5395 ± 0.0543
λ	-2.8033 ± 0.0405	-2.8644 ± 0.0751
μ	5279.9795 ± 0.0126	5279.9971 ± 0.0224
σ	8.8483 ± 0.0276	8.7861 ± 0.048
Constant parameter		
ζ	0.005	0.005
β	0	0

Table 6: Parameters of Ipatia signal fit to MC for $B^0 \rightarrow J/\psi K_S^0$

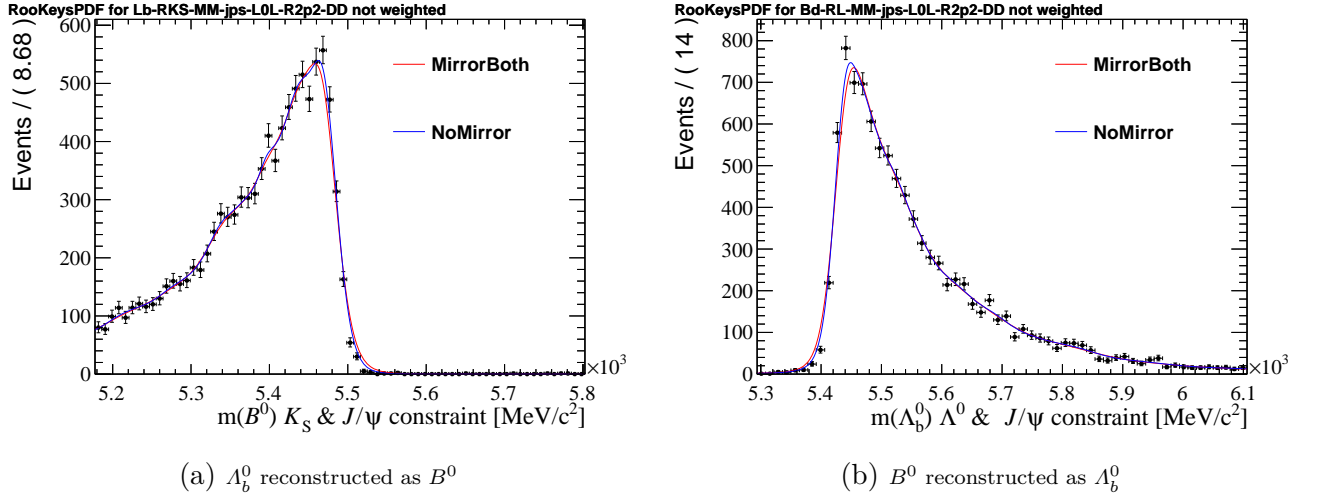


Figure 12: MisID background templates in R2p2, as determined from MC

of the ρ parameter was chosen to be 1.2. The misID background templates fitted with a RooKeysPDF in R2p2 for both Λ_b^0 reconstructed as B^0 and B^0 reconstructed as Λ_b^0 are shown in Figures 12a and 12b, respectively. For the Λ_b^0 reconstructed as B^0 , the peaking background is shifted to the right of the B^0 mass peak since the Λ_b^0 mass is larger than the B^0 mass. Conversely, the peaking background of B^0 reconstructed as Λ_b^0 is shifted to the left of the Λ_b^0 mass peak. The other misID background templates for R2p2 are given in Appendix B.

The $B_s^0 \rightarrow J/\psi K_S^0$ same final state peaking background occurs only in the B^0 mass fit and is modelled using the same Ipatia shape determined from the $B^0 \rightarrow J/\psi K_S^0$ signal shape. Since the B_s^0 mass is larger than the B^0 , the peaking background of $B_s^0 \rightarrow J/\psi K_S^0$ is shifted to the right with respect to the signal B^0 mass peak.

4.3 Combinatorial background

The combinatorial background is studied in the left and right sidebands of the signal peak for both decays and it is modelled using a simple exponential function $e^{\lambda m}$. To determine the shape of the combinatorial background, data sidebands are used instead of MC. The only parameter of this function is λ which is left floating in the fit. The value of the combinatorial exponent in the final fit is shown in Tables 7 and 8 for Λ_b^0 and B^0 fits in both R2p1 and R2p2.

4.4 Fit results

The $\Lambda_b^0 \rightarrow J/\psi \Lambda$ fit consists of a signal peak, a peaking background and a combinatorial background component. In the mass data fit, the Ipatia function parameters are fixed to those determined from the fit to MC, except for μ and σ which are left floating. The $\Lambda_b^0 \rightarrow J/\psi \Lambda$ data mass fit is performed in the range [5300,6100] MeV/ c^2 . The mass fits for R2p1 and R2p2 are shown in linear and logarithmic scale in Figure 13. The dashed red line shows the fit to the signal peak, the green peaking background is the $B^0 \rightarrow J/\psi K_S^0$ misID background and the combinatorial background is shown in blue. We note that the B^0 misID background is more significant in the Λ_b^0 fit than the analogous misID background in the B^0 fit. This is mainly due to the smaller production fraction of Λ_b^0 compared to B^0 , i.e. there are more B^0 than Λ_b^0 particles produced [15]. The results of the fit are reported in Table 7. The number of signal events is found to be 8203 ± 108 in R2p1 and 17466 ± 155 in R2p2. These results again show about a factor two between the yields in R2p1 and R2p2 which is consistent with the integrated luminosity recorded at LHCb in the two parts of Run 2.

As discussed in the previous sections, the invariant mass fit of the normalisation decay $B^0 \rightarrow J/\psi K_S^0$ consists of several fit components: signal, combinatorial background, misID background and peaking background from the $B_s^0 \rightarrow J/\psi K_S^0$ same final state decay. The invariant mass fits for R2p1 and R2p2 in both linear and logarithmic scale are shown in Figure 14. The fit of the B^0 mass is performed in the range [5180,5800] MeV/ c^2 . The dashed red line represents the fit to the signal peak, the $B_s^0 \rightarrow J/\psi K_S^0$ peaking background is shown in pink, the $\Lambda_b^0 \rightarrow J/\psi \Lambda$ misID background is shown in green and combinatorial background is shown in blue. The small background contributions from Λ_b^0 and B_s^0 are more easily observed in the logarithmic plots. The parameters μ and σ are determined in the signal peak fit to MC, but they are still left floating in the final B^0 mass fit. Table 8 reports the parameters of the final fit. The difference with respect to the value determined from the fit to MC is reported in the form of a shift parameter for μ and a scale parameter for σ . Besides the μ shift and σ scale factor, Table 8 also reports the number of signal events as well as events of each background component. The number of $B^0 \rightarrow J/\psi K_S^0$ events is found to be 43961 ± 233 for R2p1 and 92543 ± 335 for R2p2. The results agree with the integrated luminosity recorded in R2p1 and R2p2, as shown in Table 1, such that there is about a factor of two in yields between the two parts of Run 2.

Floating parameter	Fit value	
	R2p1	R2p2
Combinatorial exponent	$(-1.0416 \pm 0.0279) \times 10^{-3}$	$(-1.0929 \pm 0.0197) \times 10^{-3}$
μ shift	-0.25387 ± 0.1340	-0.088671 ± 0.0859
σ scale factor	1.1882 ± 0.0178	1.1411 ± 0.0105
$N_{B^0 \rightarrow J/\psi K_S^0}$	2969 ± 189	5195 ± 269
N_{comb}	29045 ± 249	58378 ± 357
N_{signal}	8203 ± 108	17466 ± 155

Table 7: Fit result of the binned likelihood fit to the $\Lambda_b^0 \rightarrow J/\psi \Lambda$ candidates in the two parts of the Run 2 data set

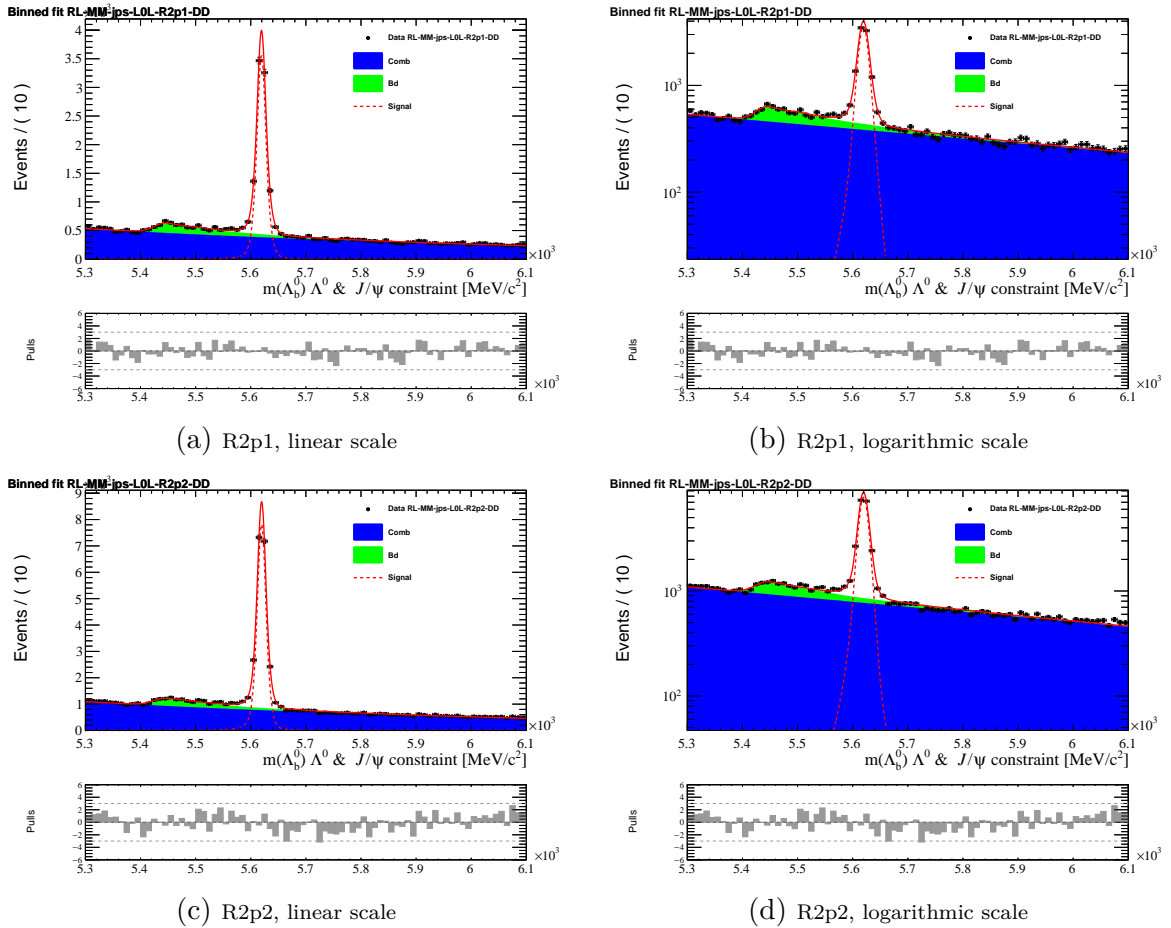


Figure 13: $\Lambda_b^0 \rightarrow J/\psi \Lambda$ mass fits for R2p1 and R2p2 in linear and logarithmic scale.

Floating parameter	Fit value	
	R2p1	R2p2
Combinatorial exponent	$(-7.3946 \pm 0.340) \times 10^{-4}$	$(-7.7346 \pm 0.244) \times 10^{-4}$
μ shift	0.089884 ± 0.0489	0.077609 ± 0.033
σ scale factor	1.1253 ± 0.00661	1.1142 ± 0.00442
$N_{B_s^0 \rightarrow J/\psi K_S^0}$	419 ± 61	900 ± 85
N_{comb}	43507 ± 325	84846 ± 456
$N_{\Lambda_b^0 \rightarrow J/\psi \Lambda}$	1485 ± 211	2518 ± 296
N_{signal}	43961 ± 233	92543 ± 335

Table 8: Fit result of the binned likelihood fit to the $B^0 \rightarrow J/\psi K_S^0$ candidates in the two parts of the Run-2 data set

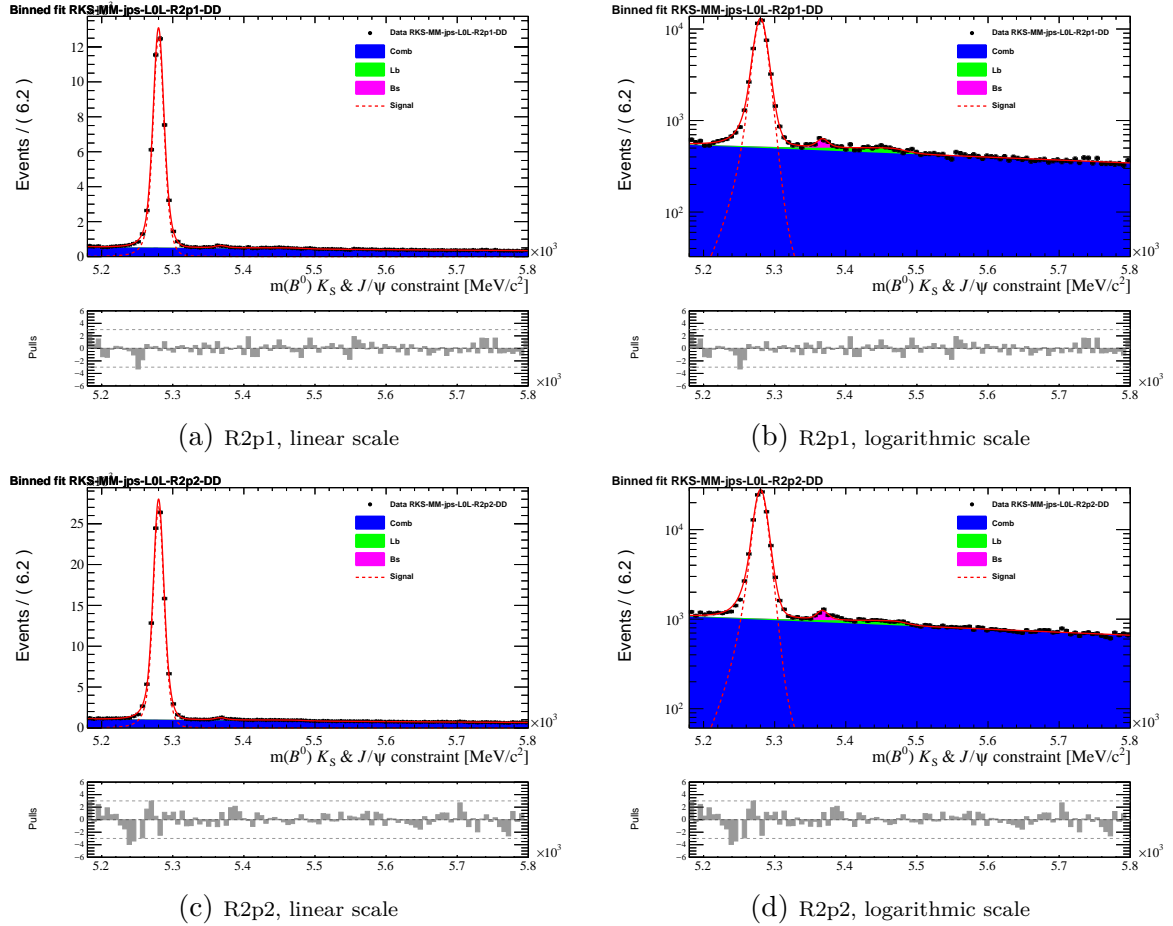


Figure 14: $B^0 \rightarrow J/\psi K_S^0$ mass fits for R2p1 and R2p2 in linear and logarithmic scale.

5 Efficiencies and MC-data corrections

This chapter discusses the determination of selection efficiencies from MC and how corrections to variables, which are inaccurately modelled in MC, are determined in order to increase the accuracy on the efficiency estimations. As shown in Equation 1, determining the signal efficiencies $\varepsilon_{\Lambda_b^0}$ and ε_{B^0} of all selection steps is needed to measure $\mathcal{B}(\Lambda_b^0 \rightarrow J/\psi \Lambda)$.

The signal efficiencies cannot be calculated from data samples, since data contains both background and signal. Therefore, efficiencies can only be calculated using MC samples. In MC simulation, all events are generated as coming from the same decay ($\Lambda_b^0 \rightarrow J/\psi \Lambda$ or $B^0 \rightarrow J/\psi K_S^0$), i.e only signal events. Furthermore, MC events are truth matched which means final state particles are required to come from the same mother particle. The efficiency of each selection is calculated by taking the ratio of signal events before and after applying the selection. The uncertainty of the efficiency is calculated as binomial error.

However, there are cases of variables that are not correctly described in simulation and thus the signal efficiency of cutting on these variables is not correctly estimated. The known cases where variables are not simulated precisely enough are: occupancy variables such as nSPDHits or nTracks, PID variables (DLL, ProbNN), L0 and HLT1 trigger variables and b-hadron kinematic variables such as p_T and η . Trigger and PID variables need to be corrected before kinematics corrections in order to get fully correct efficiency estimations. Corrections on the trigger and PID were beyond the scope of this thesis and are efficient and modelled well enough such that we only focus on correcting b-hadron kinematic variables. This is needed in order to have a better estimate of the efficiencies of the acceptance cuts on the Λ_b^0 and B^0 p_T and η .

To do this, the first step is comparing the MC distribution of these variables with the data distribution at the same selection step. Since data contains background events and we want to compare MC only with signal events, the *sPlot* tool is used to select the signal component in data for each variable [41]. The *sPlot* tool performs a mass fit with the same fit shapes as used in the nominal fit. It then estimates the number of background and signal events based on the fit and it calculates a probability of each event to be either signal or background. These probabilities are converted to weights for each event, called *sWeights*. Applying these weights to the data sample for a variable gives the signal distribution of that variable.

The purpose is to minimize the disagreement between MC and sWeighted data distributions of the b-hadron p_T and η . The typical reweighting method, the so-called histogram division, consists of simply taking the weights as a binned ratio of the two distributions. This method works well for one dimension (variable) and can sometimes work in two dimensions, but it is difficult to calculate weights in higher dimensions. It also does not take into account the correlation between variables, such as p_T and η . In addition, its stability is dependent on the number of events in each bin. A better alternative was used in this analysis, namely the **GradientBoostReweighter** (GBR) machine learning algorithm from the `hep_ml` package [42]. The GBR algorithm calculates weights that modify a certain (original) distribution to match another (target) distribution. The advantage of GBR over the histogram division method is that GBR allows for multidimensional unbinned reweighting, making it trivial to reweight p_T and η simultaneously. GBR produces a more stable reweighting while also being able to deal with correlated variables.

5.1 $B^0 \rightarrow J/\psi K_S^0$ kinematic reweighting

The reweighting of $p_T(B^0)$ and $\eta(B^0)$ is done simultaneously with the GBR. In Figure 15 sWeighted data and MC is shown for 2018 and a clear disagreement is visible in both p_T and η . Using the weights calculated by the GBR we reweight MC distributions of $p_T(B^0)$ and $\eta(B^0)$ to match sWeighted data. The reweighted distributions of the two kinematic variables are shown with blue. We can see that after the reweighting, there is a much better agreement between MC and sWeighted data in p_T and η . The B^0 kinematic reweighting also improves the data MC agreement in kinematics of the daughter particles as can be seen from the K_S^0 and one of the final state pions p_T distributions in Figure 15. However, a few χ^2 variables used in stripping, such as the vertex and IP χ^2 of B^0 (Figure 15) and daughter particles are left unaffected by the kinematic reweighting. An additional later reweighting will be needed to account for the χ^2 discrepancies. Appendix C shows the effect of the reweighting on all variables used in stripping and offline selection for $B^0 \rightarrow J/\psi K_S^0$ in 2018 data and MC. The p and p_T variables of all particles (both pions, both muons, J/ψ and K_S^0) have better agreement between MC and sWeighted data after the B^0 reweighting. The B^0 MC kinematic reweighting allows for a better estimation of ε_{B^0} and will also be used in the kinematic reweighting of Λ_b^0 as discussed in Section 5.2.

5.2 $\Lambda_b^0 \rightarrow J/\psi \Lambda$ kinematic reweighting

The kinematic reweighting of Λ_b^0 is more involved than the simple two-dimensional reweighting of B^0 , since the decay model of $\Lambda_b^0 \rightarrow J/\psi \Lambda$ must be taken into consideration. The Λ_b^0 is a baryon and has non-zero spin such that it can be produced polarized, i.e with an angular distribution. Therefore, angular corrections must be applied before any kinematic reweighting is performed on the $\Lambda_b^0 \rightarrow J/\psi \Lambda$ MC samples.

The Λ_b^0 kinematic reweighting strategy used in this thesis is based on the B^0 kinematic reweighting allowing for a decoupling from the Λ_b^0 decay model and is essentially described in the following equation [43]:

$$w(p_T, \eta) = \frac{B^0 \rightarrow J/\psi K_S^0(p_T, \eta)_{\text{data}}}{B^0 \rightarrow J/\psi K_S^0(p_T, \eta)_{\text{MC}}} \times \frac{B^0 \rightarrow J/\psi K_S^0(p_T, \eta)_{\text{gen level}}}{\Lambda_b^0 \rightarrow J/\psi \Lambda(p_T, \eta)_{\text{gen level}}} \times \frac{f_{\Lambda_b^0}}{f_d}(p_T, \eta) \quad (5)$$

In equation 5, the first term is the correction between $B^0 \rightarrow J/\psi K_S^0$ MC and data in p_T and η which was described in Section 5.1. The second term is a generator level correction in MC which is used to make the Λ_b^0 generator level MC match the B^0 generator level MC in p_T and η . The third term is the production fraction between Λ_b^0 baryons and B^0 mesons, $f_{\Lambda_b^0}/f_d$ as a function of p_T . The production fraction $f_{\Lambda_b^0}/f_d$ has no dependence on the pseudorapidity, however the η notation was included in equation 5 for consistency. The effect of the last two terms is to correct the production ratio of generator level MC between Λ_b^0 and B^0 to the actual observed production ratio, while the first term corrects for differences between data and MC in B^0 kinematics. In this way, Λ_b^0 kinematics are reweighted based on three different sets of weights.

In Figure 16, the distributions of p_T and η in generator level MC for both Λ_b^0 and B^0 are shown in red and black, respectively. A set of weights is determined with the GBR to correct Λ_b^0 generator level MC to B^0 generator level MC. The effect of applying the weights to the Λ_b^0 generator level MC in p_T and η is shown in blue. We see that the reweighted Λ_b^0 generator level MC matches perfectly to the B^0 in both p_T and η .

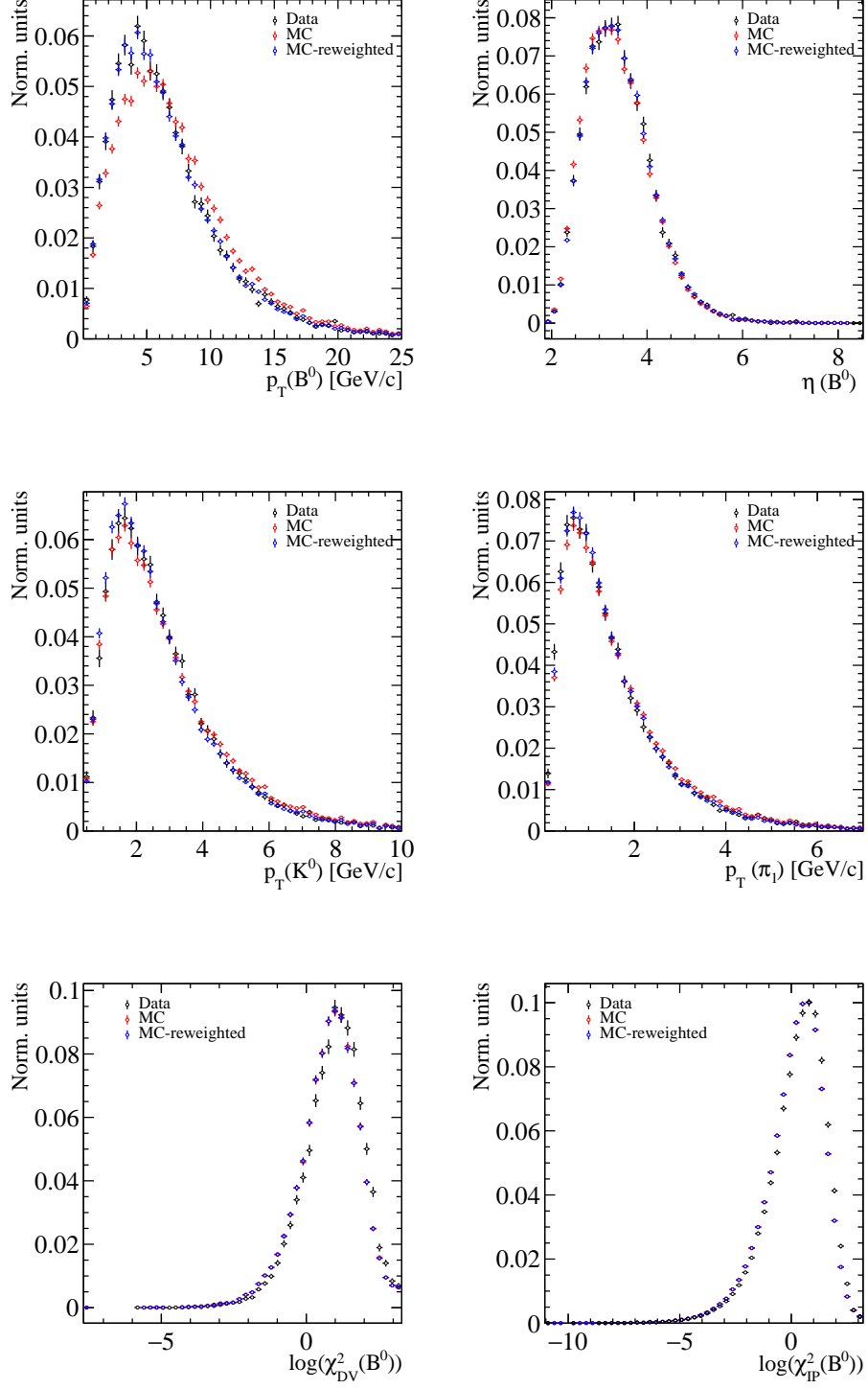


Figure 15: 2018 B^0 p_T (top left) and η (top right) MC reweighted distributions compared to sWeighted data. Also shown is the effect of the reweighting on the p_T of the K_S^0 (mid left) and on one of the final state pions (mid right). The B^0 χ^2_{DV} (bottom left) and χ^2_{IP} (bottom right) discrepancies are shown in logarithm and are unaffected by the kinematic reweighting

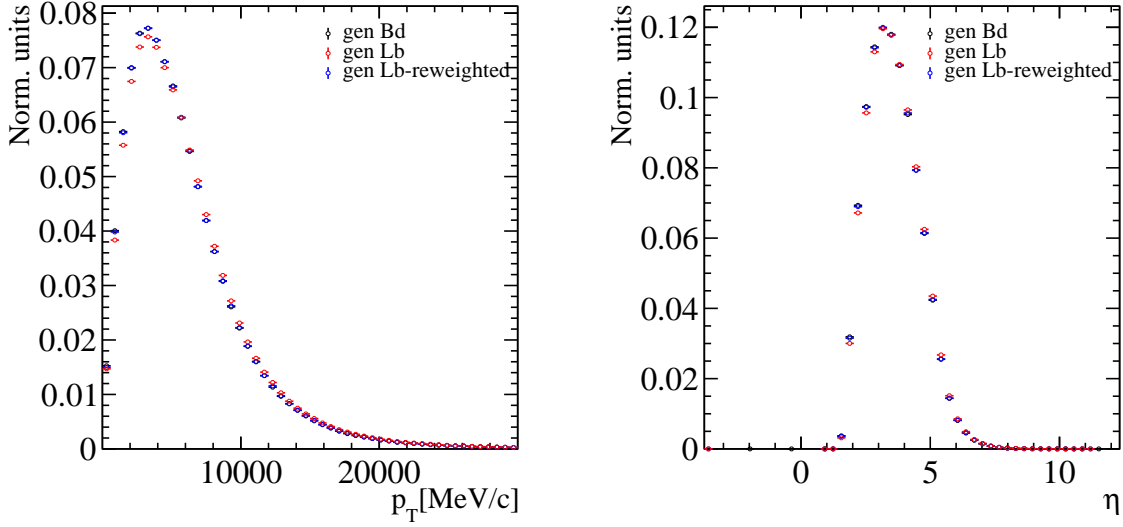


Figure 16: 2018 MC generator level corrections between Λ_b^0 and B^0 in p_T (left) and η (right). The black data points are not visible since the reweighted MC in blue overlaps perfectly.

The production fraction $f_{\Lambda_b^0}/f_d$ as a function of p_T is given in [15]. It has an exponential form:

$$\frac{f_{\Lambda_b^0}}{f_u + f_d} = A[c_1 + \exp(c_2 + c_3 \times p_T)] \quad (6)$$

with

$$\begin{aligned} A &= 1 \pm 0.061 \\ c_1 &= (7.93 \pm 1.41) \cdot 10^{-2} \\ c_2 &= -1.022 \pm 0.047 \\ c_3 &= -0.107 \pm 0.002 \text{ GeV}^{-1}. \end{aligned} \quad (7)$$

The production fraction is measured only in the fiducial p_T range [4,25] GeV. Therefore, the production fraction weights are calculated in this fiducial range per event as function of p_T according to equation 6 with parameters given in 7. As such, the Λ_b^0 kinematic reweighting is performed only in the 4-25 p_T range. The distributions of $p_T(\Lambda_b^0)$ and $\eta(\Lambda_b^0)$ in 2018 MC and sWeighted data along with the reweighted MC are shown in Figure 17. We can see that after the reweighting, there is a much better agreement between MC and data for both variables. However, at low p_T there is still a discrepancy between reweighted MC and data. This is caused by the large uncertainty of $f_{\Lambda_b^0}/f_d$ in this p_T region [15]. The Λ_b^0 kinematic reweighting improves the daughter particles kinematics as can be seen from the p_T distributions of the Λ and the final state proton before and after the reweighting in Figure 17. However, as was already observed in the B^0 reweighting, the IP and vertex χ^2 of the Λ_b^0 and daughter particles remain unaffected, as shown in Figure 17, and additional corrections will be needed to account these discrepancies.

The p_T and η reweighting effect on all variables used in stripping and offline selection is shown Appendix D for the year 2018, where MC is compared to sWeighted data before and after reweighting. In particular, this reweighting improves the match between MC and sWeighted data for all particles' p and p_T .

5.3 Efficiencies

After reweighting the b-hadron kinematics in both $B^0 \rightarrow J/\psi K_S^0$ and $\Lambda_b^0 \rightarrow J/\psi \Lambda$ MC, the weights have to be applied to the generator level MC of both B^0 and Λ_b^0 in order to obtain the corrected efficiencies ε_{B^0} and $\varepsilon_{\Lambda_b^0}$. However, this was not possible to realize in the time frame of this thesis. Instead, the uncorrected efficiencies are reported. Although the efficiencies are better estimated after applying the kinematic corrections and furthermore after applying trigger and PID corrections to MC, the uncorrected efficiencies can still provide a good first order approximation. In Table 9 the signal efficiencies of $\Lambda_b^0 \rightarrow J/\psi \Lambda$ are reported. As the MC generates events in a full solid angle of 4π , the generator level efficiency is the fraction of events that fall into the detector angular acceptance. The stripping and reconstruction efficiency is determined by comparing the generator level MC with the MC after stripping. The track type efficiency is about 76% in all years of Run 2 and it represents the efficiency of selecting only DD tracks. The L0, HLT1 and HLT2 trigger lines were given in Table 2 and are all highly efficient, with an exception of the 2015 L0 trigger due to a stronger muon p_T threshold. In particular, the 2017 L0 trigger has a higher efficiency compared to 2016 and 2018 due to a lower muon p_T threshold in MC. The hadron and lepton stripping selections should already be applied in the stripping, however due to newer versions of stripping, the selections can sometimes change. To ensure agreement with the old stripping version the stripping cuts are kept in the selection. The efficiencies of the offline selections, which was discussed in section 3.3 and summarized in Table 4 are reported next, where PID fiducial represents the efficiency of the selection on the muons p_T for PID calibration purposes while lepton PID is the `isMuon` requirement. The signal efficiencies of the Λ fiducial selection and the mass selections on the Λ and J/ψ are included. Although the Λ_b^0 fiducial selection efficiency is shown to be slightly above 70 % for all years of Run 2, this value needs to be better estimated by applying the MC corrections described in the previous section as it has been seen that uncorrected MC does not model well Λ_b^0 kinematics. The Λ_b^0 mass selection represents the signal efficiency of the mass fit range as described in section 4.4. Finally, as discussed in Chapter 4, a DTF mass variable is used to perform the fit. The DTF selection makes sure that only events where the DTF fit has converged are kept and the efficiencies are all above 90%. The corresponding efficiencies on the $B^0 \rightarrow J/\psi K_S^0$ are reported in Table 10 where the same selection steps are applied.

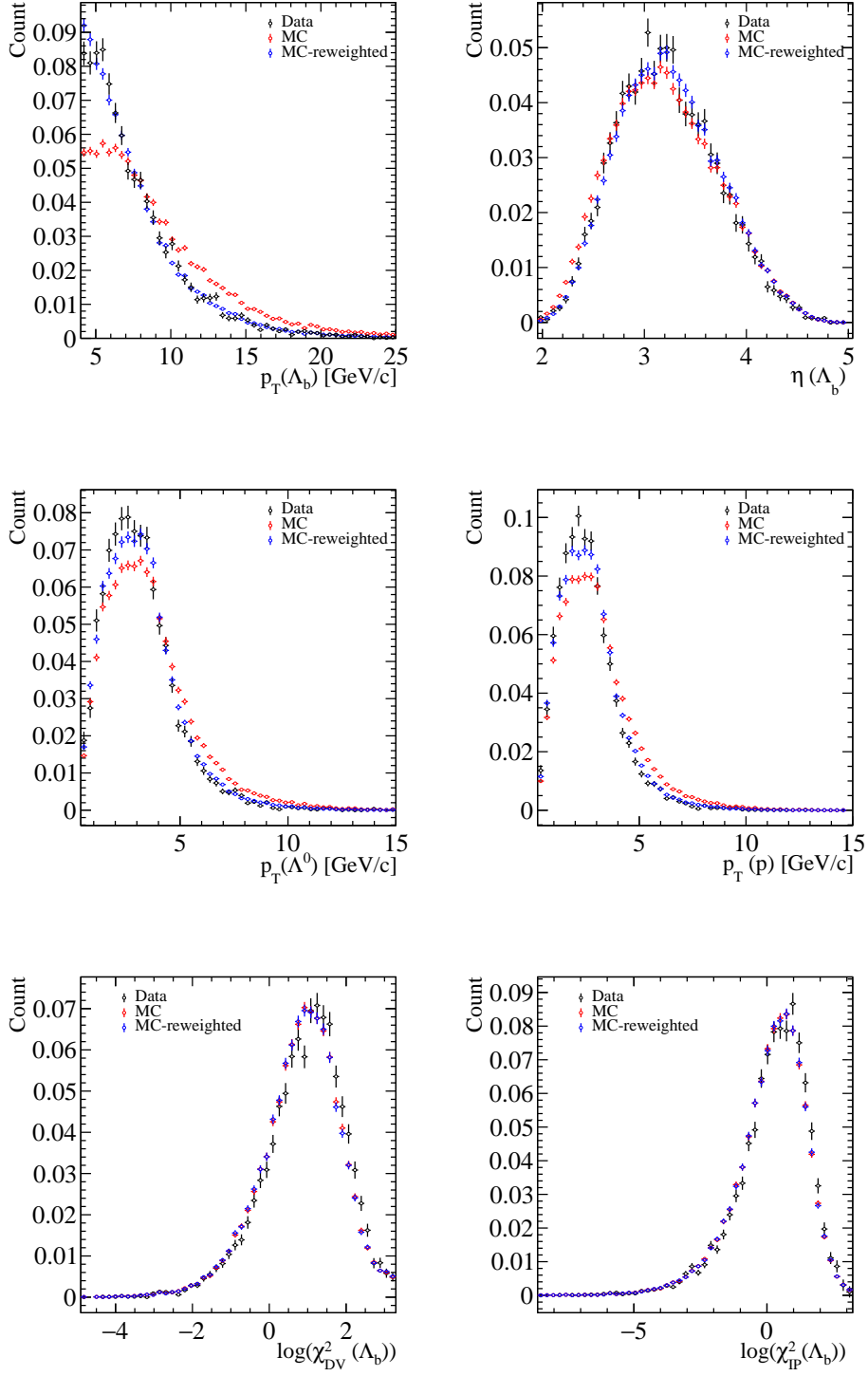


Figure 17: 2018 Λ_b^0 p_T (top left) and η (top right) MC reweighted distributions compared to sWeighted data. Also shown is the effect of the reweighting on the p_T of the Λ (mid left) and on the final state proton (mid right). The Λ_b^0 χ^2_{DV} (bottom left) and χ^2_{IP} (bottom right) discrepancies are shown in logarithm and are unaffected by the kinematic reweighting

Categories	Efficiency (%)			
	2015	2016	2017	2018
Generator level	19.83 ± 0.03	19.83 ± 0.03	19.76 ± 0.04	19.84 ± 0.05
Stripping + rec.	3.5274 ± 0.0234	3.6338 ± 0.0108	3.7057 ± 0.0108	3.6959 ± 0.0108
Track type	76.47 ± 0.29	75.57 ± 0.13	75.97 ± 0.13	76.17 ± 0.13
L0 trigger	69.69 ± 0.36	79.10 ± 0.14	83.80 ± 0.13	79.16 ± 0.14
HLT1 trigger	98.12 ± 0.13	96.13 ± 0.08	95.94 ± 0.07	96.05 ± 0.08
HLT2 trigger	98.13 ± 0.13	98.84 ± 0.04	98.67 ± 0.04	98.95 ± 0.04
Stripping hadrons	95.46 ± 0.20	97.53 ± 0.06	97.56 ± 0.06	97.58 ± 0.06
Stripping leptons	99.44 ± 0.08	99.55 ± 0.03	99.61 ± 0.03	99.57 ± 0.03
PID fiducial	97.63 ± 0.15	97.91 ± 0.06	97.80 ± 0.06	97.78 ± 0.06
Lepton PID	99.32 ± 0.08	99.39 ± 0.03	99.37 ± 0.03	99.32 ± 0.03
Λ fiducial	90.64 ± 0.29	89.40 ± 0.13	90.40 ± 0.12	90.36 ± 0.12
m_Λ selection	96.50 ± 0.19	96.35 ± 0.08	96.47 ± 0.08	96.55 ± 0.08
q^2 selection	95.07 ± 0.23	94.84 ± 0.10	94.55 ± 0.10	94.74 ± 0.10
Λ_b^0 fiducial	75.19 ± 0.47	74.00 ± 0.20	71.90 ± 0.20	73.82 ± 0.20
$m_{\Lambda_b^0}$ selection	99.62 ± 0.08	99.60 ± 0.04	99.63 ± 0.03	99.63 ± 0.03
DTF converged	93.69 ± 0.31	94.29 ± 0.12	94.45 ± 0.12	94.28 ± 0.12
Total efficiency	0.1927 ± 0.0025	0.2195 ± 0.0012	0.2325 ± 0.0013	0.2272 ± 0.013

Table 9: Efficiencies of the $\Lambda_b^0 \rightarrow J/\psi \Lambda$ signal

Categories	Efficiency (%)			
	2015	2016	2017	2018
Generator level	19.88 ± 0.03	19.82 ± 0.02	19.77 ± 0.02	19.78 ± 0.03
Stripping + rec.	6.6599 ± 0.0078	6.8276 ± 0.0108	6.9744 ± 0.0215	6.9690 ± 0.0106
Track type	72.28 ± 0.05	71.59 ± 0.05	71.98 ± 0.14	72.32 ± 0.07
L0 trigger	70.03 ± 0.06	79.79 ± 0.05	84.52 ± 0.14	80.01 ± 0.07
HLT1 trigger	98.40 ± 0.02	96.18 ± 0.03	96.00 ± 0.08	96.19 ± 0.04
HLT2 trigger	98.56 ± 0.02	99.11 ± 0.01	98.96 ± 0.04	99.12 ± 0.02
Stripping hadrons	98.66 ± 0.02	99.39 ± 0.01	99.53 ± 0.03	99.35 ± 0.02
Stripping leptons	99.60 ± 0.01	99.62 ± 0.01	99.69 ± 0.02	99.61 ± 0.01
PID fiducial	97.86 ± 0.03	97.95 ± 0.02	97.96 ± 0.06	97.88 ± 0.03
Lepton PID	100.00 ± 0.00	100.00 ± 0.00	100.00 ± 0.00	100.00 ± 0.00
K_S^0 fiducial	96.52 ± 0.03	95.87 ± 0.03	96.00 ± 0.08	95.97 ± 0.04
$m_{K_S^0}$ selection	92.41 ± 0.05	92.34 ± 0.04	92.77 ± 0.11	92.47 ± 0.06
q^2 selection	95.24 ± 0.04	94.71 ± 0.03	94.78 ± 0.10	94.68 ± 0.05
B^0 fiducial	76.09 ± 0.08	73.35 ± 0.07	71.15 ± 0.21	73.61 ± 0.10
m_{B^0} selection	99.30 ± 0.02	99.27 ± 0.02	99.33 ± 0.05	99.29 ± 0.02
DTF converged	92.82 ± 0.06	92.84 ± 0.05	93.76 ± 0.13	91.98 ± 0.08
Total efficiency	0.3723 ± 0.0009	0.4050 ± 0.0010	0.4332 ± 0.0024	0.4160 ± 0.0013

Table 10: Efficiencies of the $B^0 \rightarrow J/\psi K_S^0$ signal

6 Results

As discussed in Section 1.2, the $\Lambda_b^0 \rightarrow J/\psi \Lambda$ branching fraction is calculated through the following equation

$$\mathcal{B}(\Lambda_b^0 \rightarrow J/\psi \Lambda) = \mathcal{B}(B^0 \rightarrow J/\psi K_S^0) \times \frac{f_d}{f_{\Lambda_b^0}} \times \frac{N_{\Lambda_b^0}}{N_{B^0}} \times \frac{\varepsilon_{B^0}}{\varepsilon_{\Lambda_b^0}} \times \frac{\mathcal{B}(K_S^0 \rightarrow \pi^+ \pi^-)}{\mathcal{B}(\Lambda \rightarrow p \pi^-)} \quad (8)$$

where the signal yields $N_{\Lambda_b^0}$ and N_{B^0} are obtained from invariant mass fits as shown in Chapter 4 and the efficiencies $\varepsilon_{\Lambda_b^0}$ and ε_{B^0} as shown in Chapter 5. Table 11 shows the $\Lambda_b^0 \rightarrow J/\psi \Lambda$ and $B^0 \rightarrow J/\psi K_S^0$ efficiencies, signal yields and efficiency corrected yields in R2p1 and R2p2.

Parameter	R2p1	R2p2
$\varepsilon_{\Lambda_b^0}$ (%)	0.2150 ± 0.0014	0.2295 ± 0.0012
ε_{B^0} (%)	0.3995 ± 0.0009	0.4237 ± 0.0017
$N_{\Lambda_b^0}$	8203 ± 108	17466 ± 155
N_{B^0}	43961 ± 233	92543 ± 335
$N_{\Lambda_b^0}/\varepsilon_{\Lambda_b^0}$	$(3.80 \pm 0.05) \times 10^6$	$(7.55 \pm 0.07) \times 10^6$
$N_{B^0}/\varepsilon_{B^0}$	$(1.105 \pm 0.006) \times 10^7$	$(2.189 \pm 0.011) \times 10^7$

Table 11: Efficiencies, yields and corrected yields in R2p1 and R2p2

The branching fraction of $B^0 \rightarrow J/\psi K_S^0$ is assumed to be 50% of the branching fraction of $B^0 \rightarrow J/\psi K^0$, which is taken from the PDG [14]. Therefore, the following value is used:

$$\mathcal{B}(B^0 \rightarrow J/\psi K_S^0) = (4.34 \pm 0.15) \times 10^{-4} \quad (9)$$

The branching ratios of $K_S^0 \rightarrow \pi^+ \pi^-$ and $\Lambda \rightarrow p \pi^-$ are also taken from the PDG [14] to be:

$$\mathcal{B}(K_S^0 \rightarrow \pi^+ \pi^-) = 0.6920 \pm 0.0005 \quad (10)$$

and

$$\mathcal{B}(\Lambda \rightarrow p \pi^-) = 0.639 \pm 0.005 \quad (11)$$

The relative production fraction $f_{\Lambda_b^0}/(f_d + f_u)$ is reported in the fiducial p_T range 4-25 GeV/c. The production fraction shows an exponential p_T dependence. Due to a limited time, an appropriate implementation of the p_T dependence of the production fraction in the final result was not possible. Instead, the average over the 4-25 GeV/c p_T range is used as a single value in the computation of the $\Lambda_b^0 \rightarrow J/\psi \Lambda$ branching fraction. The average value is:

$$\frac{f_{\Lambda_b^0}}{f_d + f_u} = 0.259 \pm 0.018 \quad (12)$$

In the assumption that $f_d = f_u$, the relative production fraction $f_{\Lambda_b^0}/f_d$ needed for the calculation in Equation 8 has an additional factor of 2.

Combining all the necessary inputs in Equation 8, and summing over the efficiency corrected yields of R2p1 and R2p2, gives a value on the $\Lambda_b^0 \rightarrow J/\psi \Lambda$ branching fraction of:

$$\mathcal{B}(\Lambda_b^0 \rightarrow J/\psi \Lambda) = (2.67 \pm 0.03 \text{ (stat)} \pm 0.18 (f_{\Lambda_b^0}/f_d) \pm 0.09 (\mathcal{B})) \times 10^{-4} \quad (13)$$

where the uncertainties are the statistical uncertainty, the uncertainty on the relative production fractions, and the uncertainty on the external branching fractions, respectively. It can be seen that the highest contribution to the uncertainty comes from the $f_{\Lambda_b^0}/f_d$ production fraction uncertainty. However, this uncertainty is an estimate and it can change depending on the method used to implement $f_{\Lambda_b^0}/f_d$ in the $\mathcal{B}(\Lambda_b^0 \rightarrow J/\psi \Lambda)$ measurement, as discussed in Section 7.1.

This result is the most precise measurement of $\mathcal{B}(\Lambda_b^0 \rightarrow J/\psi \Lambda)$ to date and the first measurement of this branching fraction performed at the LHC. This result is consistent with the latest estimation of $\mathcal{B}(\Lambda_b^0 \rightarrow J/\psi \Lambda) = (3.7 \pm 1.0) \times 10^{-4}$ based on the D0 measurement [44]. However, its uncertainty of about 8% is improved by more than a factor 3 with respect to the existing measurement by the D0 collaboration.

The presented result does not take into account systematic uncertainties. An overview of the systematic uncertainties is given in the following section.

6.1 Systematic uncertainties

A study of the systematic uncertainties is foreseen, and an overview on possible sources of systematic uncertainties is given below.

- **Signal fit shape.** In this analysis, the signal peaks for both $\Lambda_b^0 \rightarrow J/\psi \Lambda$ and $B^0 \rightarrow J/\psi K_S^0$ are modelled with an Ipatia function. However, using a different signal shape can yield a slightly different result. A possibility is to fit the signal using a Double Sided Crystal Ball (DSCB) which consists of a Gaussian core with exponential tails [45].
- **Peaking background shapes.** The other source of systematic errors associated with the fit model consists of using different shapes to model the peaking backgrounds. Firstly, the ρ parameter of the RooKeysPDF shape can be varied. The choice of this parameter can affect both the signal and the background yields. An alternative to the RooKeysPDF used in this analysis is the RooMisID [46] package for fitting misidentified backgrounds, which takes into account the analytical relation between the true mass and the misidentified mass.
- **Reweighting.** The Λ_b^0 kinematics reweighting approach used in this thesis allows for a decoupling from the Λ_b^0 decay model. However, the data-MC discrepancies can also be resolved by firstly correcting for the decay model, i.e. angular corrections, and then performing a two dimensional reweighting in p_T and η with the GBR. In this way, a direct reweighting of the Λ_b^0 kinematics can be performed.
- **Data-MC discrepancies.** Even after the kinematic reweighting is performed, some variables still show data-MC discrepancies, such as the χ_{IP}^2 and χ_{vtx}^2 variables. Moreover, the kinematic variable distributions are not perfectly corrected for. This introduces a systematic error in the calculation of the signal efficiencies.

The systematic uncertainties sources given above are experimental and they affect the uncertainties on the quantities measured in this analysis, i.e. the yields $N_{\Lambda_b^0}$, N_{B^0} and the efficiencies $\varepsilon_{\Lambda_b^0}$ and ε_{B^0} . There are also external sources of systematic uncertainties, namely the uncertainties on the branching fractions and production fraction used to convert the measured quantities into the branching fraction $\mathcal{B}(\Lambda_b^0 \rightarrow J/\psi \Lambda)$. These are the uncertainties on the branching fractions $\mathcal{B}(\Lambda \rightarrow p\pi^-)$, $\mathcal{B}(K_S^0 \rightarrow \pi^-\pi^+)$, $\mathcal{B}(B^0 \rightarrow J/\psi K_S^0)$ and on the production fraction $f_{\Lambda_b^0}/f_d$. We note that the systematic uncertainties on $f_{\Lambda_b^0}/f_d$ and the branching ratios together give an uncertainty of almost 8%. Therefore, these external systematic uncertainties are the limitation to the precision of measurement performed in this thesis. More precise measurements of both the production fraction and the normalisation channel branching fraction are needed to further reduce the uncertainty on $\mathcal{B}(\Lambda_b^0 \rightarrow J/\psi \Lambda)$.

7 Conclusion and outlook

In this thesis, a measurement of the $\mathcal{B}(\Lambda_b^0 \rightarrow J/\psi \Lambda)$ normalized to the $\mathcal{B}(B^0 \rightarrow J/\psi K_S^0)$ branching fraction using the full Run 2 dataset taken with the LHCb detector is performed. The yields of the decays $\Lambda_b^0 \rightarrow J/\psi \Lambda$ and $B^0 \rightarrow J/\psi K_S^0$ were determined in the R2p1 and R2p2 data samples. The signal efficiencies of both decay channels were determined from MC samples. Discrepancies between sWeighted data and MC in Λ_b^0/B^0 p_T and η were corrected for in order to have a better estimation of the efficiencies. The efficiency corrected yields for R2p1 and R2p2 were combined and the $\Lambda_b^0 \rightarrow J/\psi \Lambda$ branching fraction was computed as $\mathcal{B}(\Lambda_b^0 \rightarrow J/\psi \Lambda) = (2.67 \pm 0.03 \text{ (stat)} \pm 0.18 (f_{\Lambda_b^0}/f_d) \pm 0.09 (\mathcal{B})) \times 10^{-4}$. This result is the most precise to date and it is compatible with the previous measurements. The large uncertainties of previous measurements were due to the lack of knowledge of the Λ_b^0 production fraction. The uncertainty of the measurement presented in this thesis is greatly reduced with respect to the previous ones; however the dominant source of uncertainty is still the $f_{\Lambda_b^0}/f_d$ production fraction. As discussed in Chapter 1, a more precise measurement of the $\mathcal{B}(\Lambda_b^0 \rightarrow J/\psi \Lambda)$ will help reduce the uncertainties in the $\Lambda_b^0 \rightarrow \mu^+ \mu^-$ measurement and will also be used as normalization channel in the search for the LFV $\Lambda_b^0 \rightarrow e^\pm \mu^\mp$ analysis, further constraining contributions from New Physics in rare decays of b hadrons.

7.1 Outlook

There are still a few steps to be done in this analysis in order to obtain the final measurement of the $\mathcal{B}(\Lambda_b^0 \rightarrow J/\psi \Lambda)$.

First of all, the obtained data-MC corrections for both $\Lambda_b^0 \rightarrow J/\psi \Lambda$ and $B^0 \rightarrow J/\psi K_S^0$ kinematics have to be applied to the generator level MC to get a better calculation of the efficiencies. Additional corrections can be performed for the variables that are still not well modelled, such as χ_{IP}^2 and χ_{vtx}^2 .

Besides b -hadron kinematics, L0 and HLT1 trigger corrections are needed to have a better estimate on the trigger efficiency. Trigger corrections can be obtained using the TISTOS method [47]. In this method, trigger efficiency is determined in data and MC in bins on the maximum of the two muons p_T and the product of the two muons p_T . The MC is then reweighted using the resulting two-dimensional histogram.

PID corrections must also be taken into account as MC does not model the data correctly for this type of variables. In this analysis, the only PID variable used is `isMuon` and an accurate efficiency estimation of this cut is desired. Corrections can be obtained using the PIDCalib package. [48]

The Λ_b^0 baryon lifetime has to be corrected to be consistent with the most recent measurements. Thus, an analytical reweighting of the $\tau(\Lambda_b^0)$ variable is needed.

A Boosted Decision Tree (BDT) can be used in the analysis to further reduce background. The BDT will have several variables as input. In case the input variables are not correctly modelled in MC, the efficiency of the BDT cut will have to be taken into account in the systematic uncertainties.

In this thesis, the relative production fraction $f_{\Lambda_b^0}/f_d$ has been accounted for by simply using the averaged value over the 4-25 GeV/ c p_T range. However, the p_T dependence of $f_{\Lambda_b^0}/f_d$ requires a more careful implementation of the production fraction in the measurement of $\mathcal{B}(\Lambda_b^0 \rightarrow J/\psi \Lambda)$. There are two approaches to account for this additional

complication. One way is to work in bins of p_T and therefore measure $\mathcal{B}(\Lambda_b^0 \rightarrow J/\psi \Lambda)$ for each p_T bin. However, the alternative approach planned to use in this analysis is to treat $f_{\Lambda_b^0}/f_d$ as a per-event weight using the known exponential function. In this way, a p_T dependent reweighting will be performed and corrected signal yields will be extracted.

Finally, a study of the experimental systematic errors has to be performed. Usually, pseudoexperiments are performed in which the parameters of one possible source of systematic uncertainties are varied. An estimation of the experimental systematic uncertainties can be found in [7]. It is expected that the systematic uncertainty on the yields does not exceed 1% while the systematic uncertainty on the efficiencies does not exceed 3%. Therefore, the dominant source of systematic uncertainties are the external normalisation channel branching fraction $\mathcal{B}(B^0 \rightarrow J/\psi K_S^0)$ and the production fraction $f_{\Lambda_b^0}/f_d$.

References

- [1] S. L. Glashow, *Partial Symmetries of Weak Interactions*, **Nucl. Phys.** **22** (1961) 579.
- [2] S. Weinberg, *A Model of Leptons*, **Phys. Rev. Lett.** **19** (1967) 1264.
- [3] A. Salam, *Weak and Electromagnetic Interactions*, **Conf. Proc. C** **680519** (1968) 367.
- [4] Wikipedia, https://en.wikipedia.org/wiki/standard_model, Accessed: 24-06-2020.
- [5] G. Chatzikonstantinidis, *Angular Analysis of $\Lambda_b^0 \rightarrow \Lambda \mu^+ \mu^-$ and $\Lambda_b^0 \rightarrow J/\psi \Lambda$ decays with the LHCb detector*, CERN, PhD Thesis, University of Birmingham, 2019.
- [6] S. L. Glashow, J. Iliopoulos, and L. Maiani, *Weak interactions with lepton-hadron symmetry*, **Phys. Rev. D** **2** (1970) 1285.
- [7] LHCb collaboration, R. Aaij *et al.*, *Differential branching fraction and angular analysis of $\Lambda_b^0 \rightarrow \Lambda \mu^+ \mu^-$ decays*, **JHEP** **06** (2015) 115, Erratum *ibid.* **09** (2018) 145, [arXiv:1503.07138](#).
- [8] M. Algueró *et al.*, *Emerging patterns of new physics with and without lepton flavour universal contributions*, **The European Physical Journal C** **79** (2019) .
- [9] J. Aebischer *et al.*, *B-decay discrepancies after moriond 2019*, **The European Physical Journal C** **80** (2020) .
- [10] W. Detmold and S. Meinel, *$\Lambda_b^0 \rightarrow \Lambda l^+ l^-$ form factors, differential branching fraction, and angular observables from lattice QCD with relativistic b quarks*, **Physical Review D** **93** (2016) .
- [11] S. Sahoo and R. Mohanta, *Effects of scalar leptoquark on semileptonic Λ_b^0 decays*, **New Journal of Physics** **18** (2016) 093051.
- [12] D0 collaboration, V. M. Abazov *et al.*, *Measurement of the production fraction times branching fraction $f(b \rightarrow \Lambda_b) \cdot \mathcal{B}(\Lambda_b \rightarrow J/\psi \Lambda)$* , **Physical Review D** **84** (2011) .
- [13] LHCb Collaboration, <http://lhcb-public.web.cern.ch/>, .
- [14] Particle Data Group, M. Tanabashi *et al.*, *Review of particle physics*, **Phys. Rev. D** **98** (2018) 030001, and 2019 update.
- [15] LHCb collaboration, R. Aaij *et al.*, *Measurement of b -hadron fractions in 13 TeV pp collisions*, **Phys. Rev. D** **101** (2019) 031102(R), [arXiv:1902.06794](#).
- [16] L. Evans and P. Bryant, *LHC Machine*, **JINST** **3** (2008), no. 08 S08001.
- [17] A. Hoecker, *Physics at the lhc run-2 and beyond*, [arXiv:1611.07864](#).
- [18] ATLAS collaboration, G. Aad *et al.*, *The ATLAS experiment at the CERN large hadron collider*, **Journal of Instrumentation** **3** (2008) S08003.
- [19] CMS collaboration, S. Chatrchyan *et al.*, *The CMS experiment at the CERN LHC*, **Journal of Instrumentation** **3** (2008) S08004.

- [20] ALICE collaboration, K. Aamodt *et al.*, *The ALICE experiment at the CERN LHC*, [Journal of Instrumentation](#) **3** (2008) S08002.
- [21] LHCb collaboration, A. A. Alves Jr. *et al.*, *The LHCb detector at the LHC*, [JINST](#) **3** (2008) S08005.
- [22] LHCb collaboration, *LHCb VELO (Vertex Locator): Technical Design Report*, [CERN-LHCC-2001-011](#), 2001.
- [23] LHCb collaboration, R. Aaij *et al.*, *LHCb detector performance*, [Int. J. Mod. Phys. A](#) **30** (2015) 1530022, [arXiv:1412.6352](#).
- [24] LHCb collaboration, *LHCb inner tracker: Technical Design Report*, [CERN-LHCC-2002-029](#), 2002.
- [25] LHCb collaboration, *LHCb outer tracker: Technical Design Report*, [CERN-LHCC-2001-024](#), 2001.
- [26] LHCb collaboration, *LHCb magnet: Technical Design Report*, [CERN-LHCC-2000-007](#), 2000.
- [27] LHCb collaboration, R. Aaij *et al.*, *Measurement of the track reconstruction efficiency at LHCb*, [JINST](#) **10** (2015) P02007, [arXiv:1408.1251](#).
- [28] LHCb collaboration, *LHCb calorimeters: Technical Design Report*, [CERN-LHCC-2000-036](#), 2000.
- [29] LHCb collaboration, *LHCb RICH: Technical Design Report*, [CERN-LHCC-2000-037](#), 2000.
- [30] LHCb collaboration, *LHCb muon system: Technical Design Report*, [CERN-LHCC-2001-010](#), 2001.
- [31] LHCb collaboration, *LHCb trigger system: Technical Design Report*, [CERN-LHCC-2003-031](#), 2003.
- [32] LHCb collaboration, *LHCb Trigger and Online Technical Design Report*, [CERN-LHCC-2014-016](#), 2014.
- [33] LHCb, F. Dordei, *LHCb detector and trigger performance in Run II*, [EPJ Web Conf.](#), **164** (2017) 01016. 10 p.
- [34] R. Aaij *et al.*, *Performance of the LHCb trigger and full real-time reconstruction in Run 2 of the LHC*, [JINST](#) **14** (2019) P04013, [arXiv:1812.10790](#).
- [35] F. Archilli *et al.*, *Performance of the muon identification at LHCb*, [JINST](#) **8** (2013) P10020, [arXiv:1306.0249](#).
- [36] W. Verkerke and D. Kirkby, *The roofit toolkit for data modeling*, [arXiv:physics/0306116](#).
- [37] R. Brun and F. Rademakers, *ROOT: An object oriented data analysis framework*, [Nucl. Instrum. Meth. A](#) **389** (1997) 81.

- [38] W. D. Hulsbergen, *Decay chain fitting with a kalman filter*, *Nuclear Instruments and Methods in Physics Research Section A: Accelerators, Spectrometers, Detectors and Associated Equipment* **552** (2005) 566–575.
- [39] D. Martínez Santos and F. Dupertuis, *Mass distributions marginalized over per-event errors*, *Nuclear Instruments and Methods in Physics Research Section A: Accelerators, Spectrometers, Detectors and Associated Equipment* **764** (2014) 150–155.
- [40] K. Cranmer, *Kernel estimation in high-energy physics*, *Computer Physics Communications* **136** (2001) 198–207.
- [41] M. Pivk and F. R. Le Diberder, : *A statistical tool to unfold data distributions*, *Nuclear Instruments and Methods in Physics Research Section A: Accelerators, Spectrometers, Detectors and Associated Equipment* **555** (2005) 356–369.
- [42] A. Rogozhnikov, https://arogozhnikov.github.io/hep_ml/reweight.html, Accessed: 24-06-2020.
- [43] LHCb collaboration, R. Aaij *et al.*, *Measurement of the $\Lambda_b^0 \rightarrow J/\psi \Lambda$ angular distribution and the Λ_b^0 polarisation in pp collisions*, [arXiv:2004.10563](https://arxiv.org/abs/2004.10563), submitted to JHEP.
- [44] T. Blake, S. Meinel, and D. van Dyk, *Bayesian analysis of $b \rightarrow s\mu^+\mu^-$ Wilson coefficients using the full angular distribution $\Lambda_b^0 \rightarrow \Lambda(\rightarrow p\pi^-)\mu^+\mu^-$ decays*, *Physical Review D* **101** (2020) .
- [45] T. Skwarnicki, *A study of the radiative cascade transitions between the Upsilon-prime and Upsilon resonances*, PhD thesis, Institute of Nuclear Physics, Krakow, 1986, [DESY-F31-86-02](#).
- [46] M. van Veghel, <https://github.com/maartenvanv/roomisid/tree/master/src>, Accessed: 24-06-2020.
- [47] S. Tolk, J. Albrecht, F. Dettori, and A. Pellegrino, *Data driven trigger efficiency determination at LHCb*, [LHCb-PUB-2014-039](#), 2014.
- [48] L. Anderlini *et al.*, *The PIDCalib package*, [LHCb-PUB-2016-021](#), 2016.

Appendices

A Preselection plots

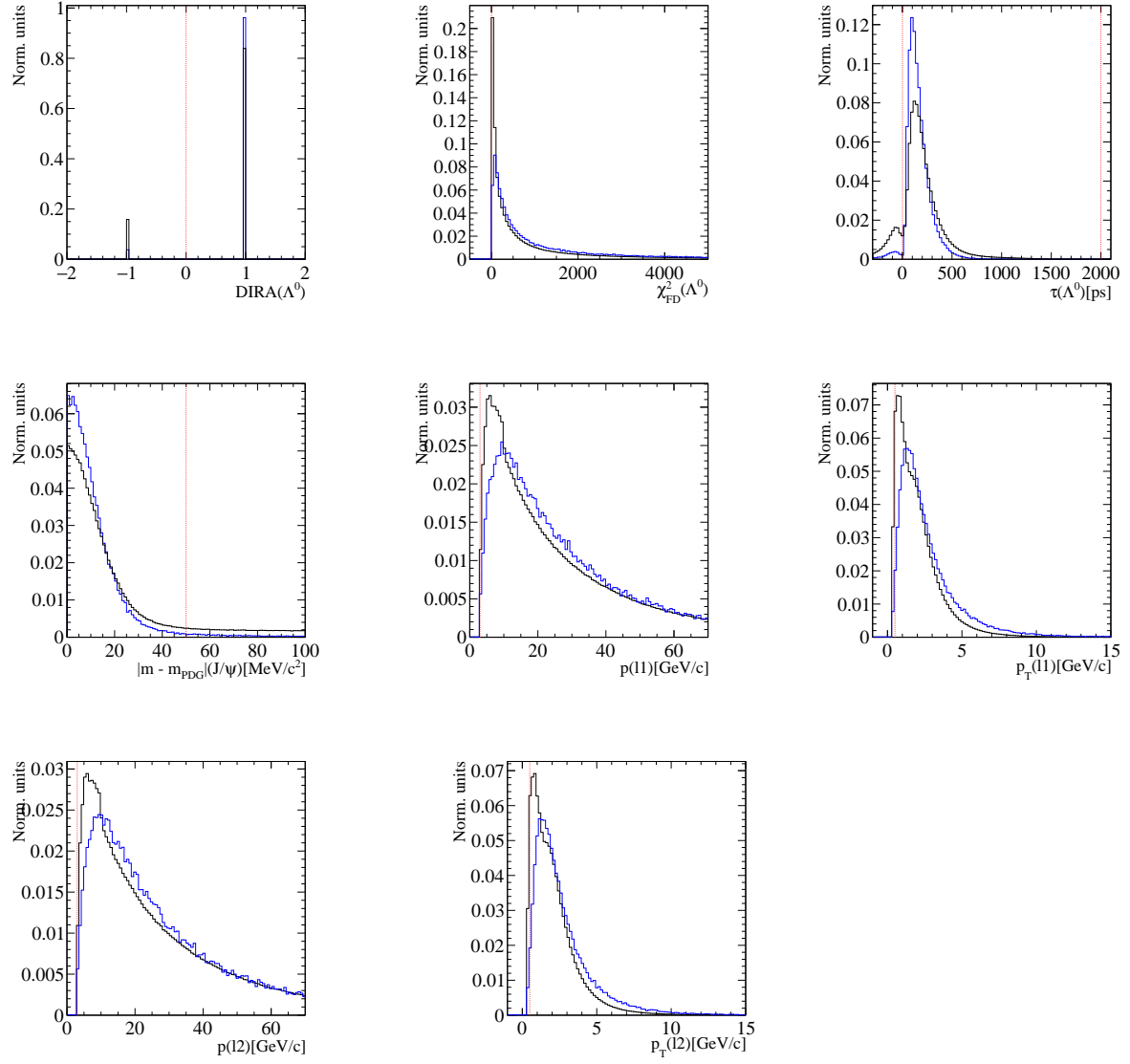


Figure 18: Offline selection for $\Lambda_b^0 \rightarrow J/\psi \Lambda$

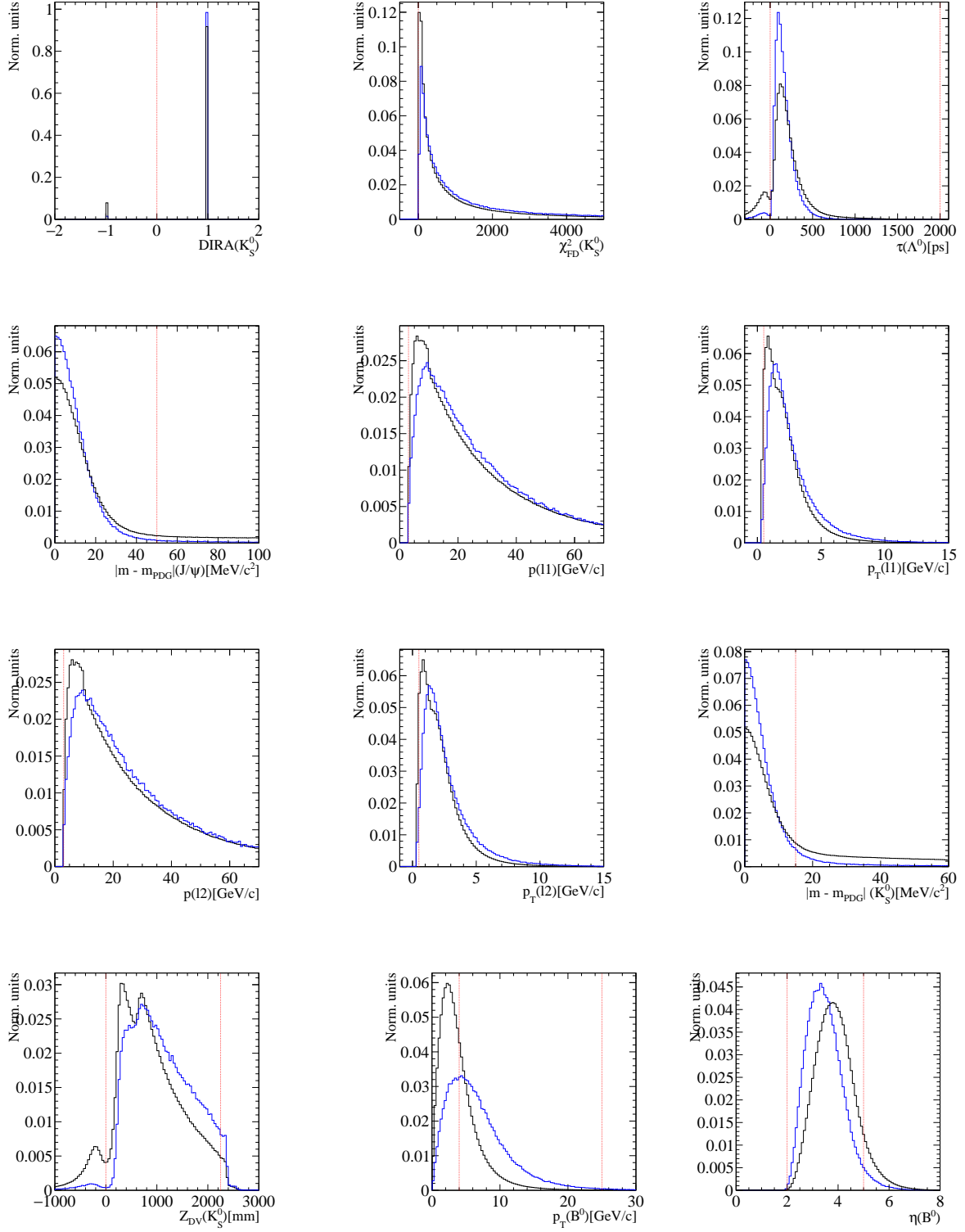


Figure 19: Offline selection for $B^0 \rightarrow J/\psi K_S^0$

B Fit Monte-Carlo templates

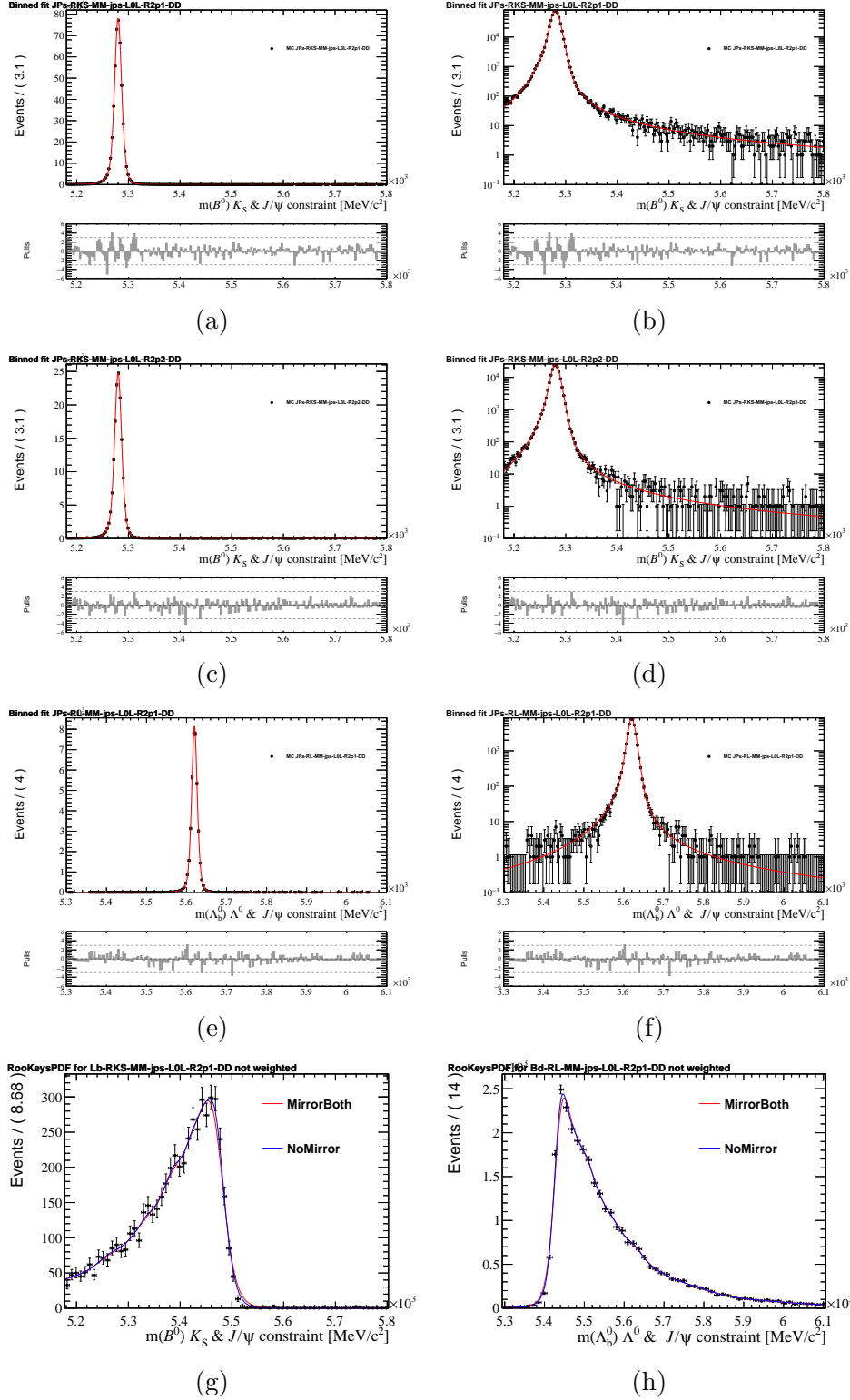


Figure 20: B^0 and Λ_b^0 signal fits are shown in linear and log scale in (a), (b) and (e), (f) in R2p1 and in (c), (d) in R2p2. MisID background templates in R2p1 are shown in (g) and (h)

C Reweighted variables $\Lambda_b^0 \rightarrow J/\psi \Lambda$

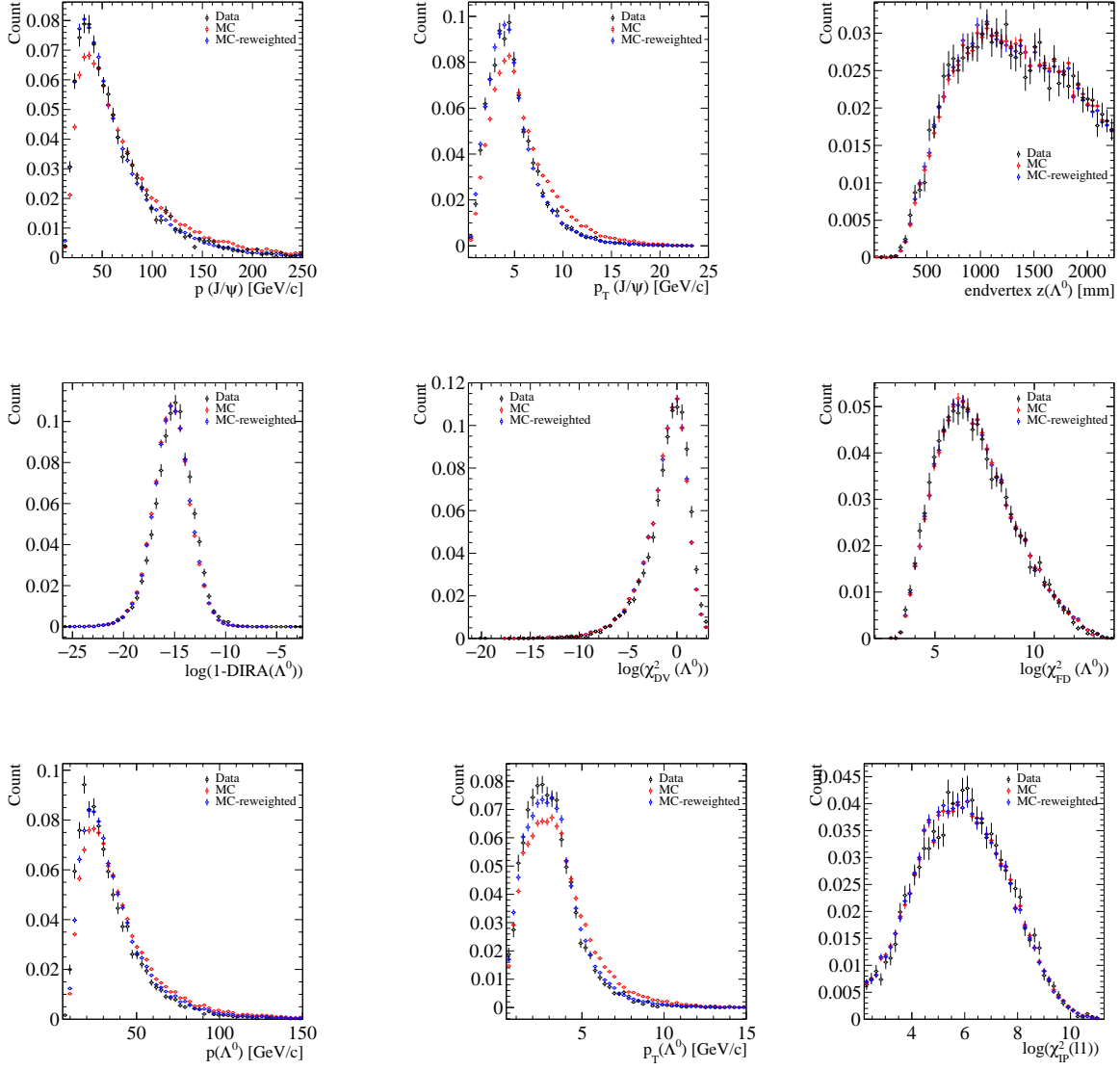


Figure 21: 2018 reweighted variables for $\Lambda_b^0 \rightarrow J/\psi \Lambda$

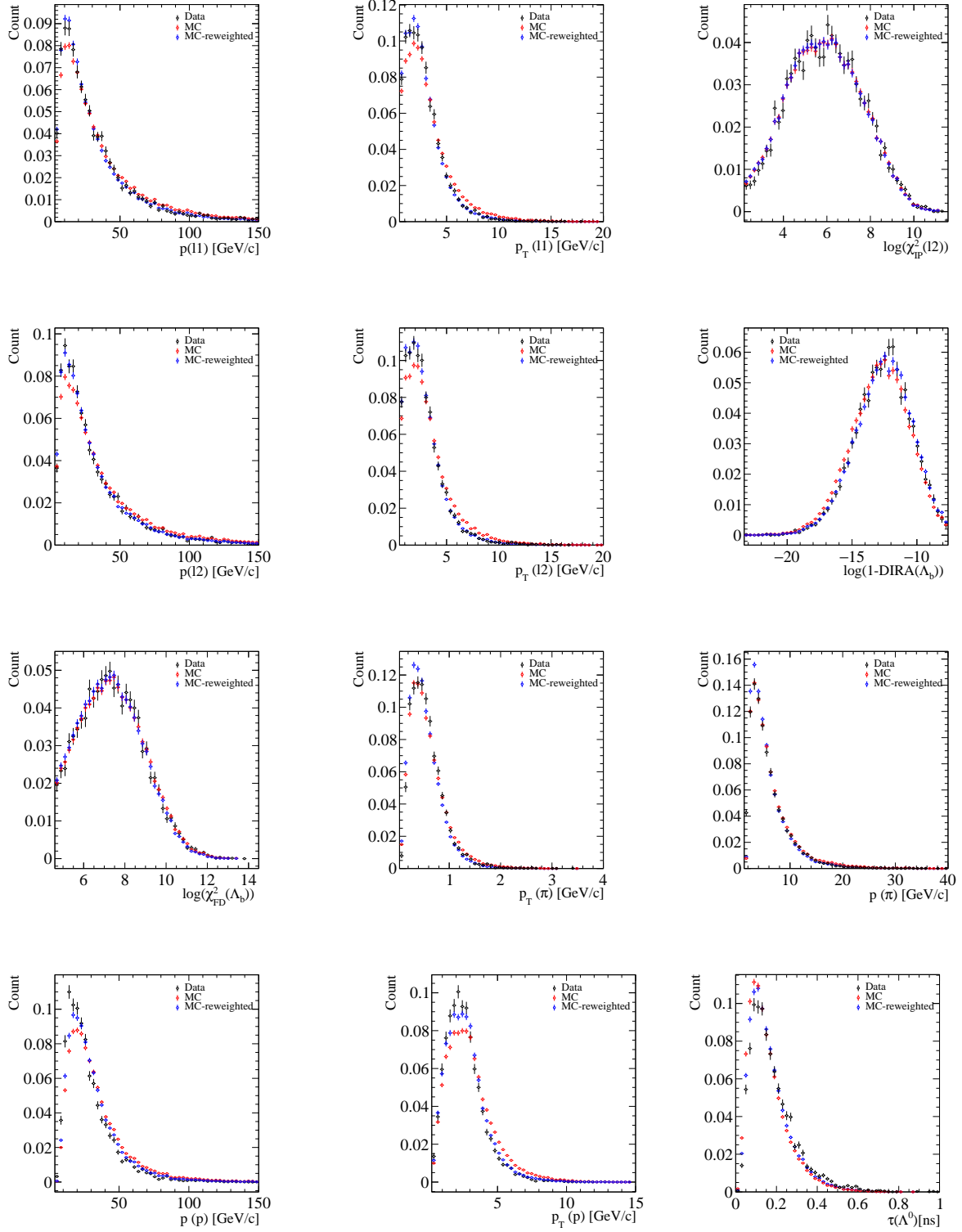


Figure 22: 2018 reweighted variables for $\Lambda_b^0 \rightarrow J/\psi \Lambda$

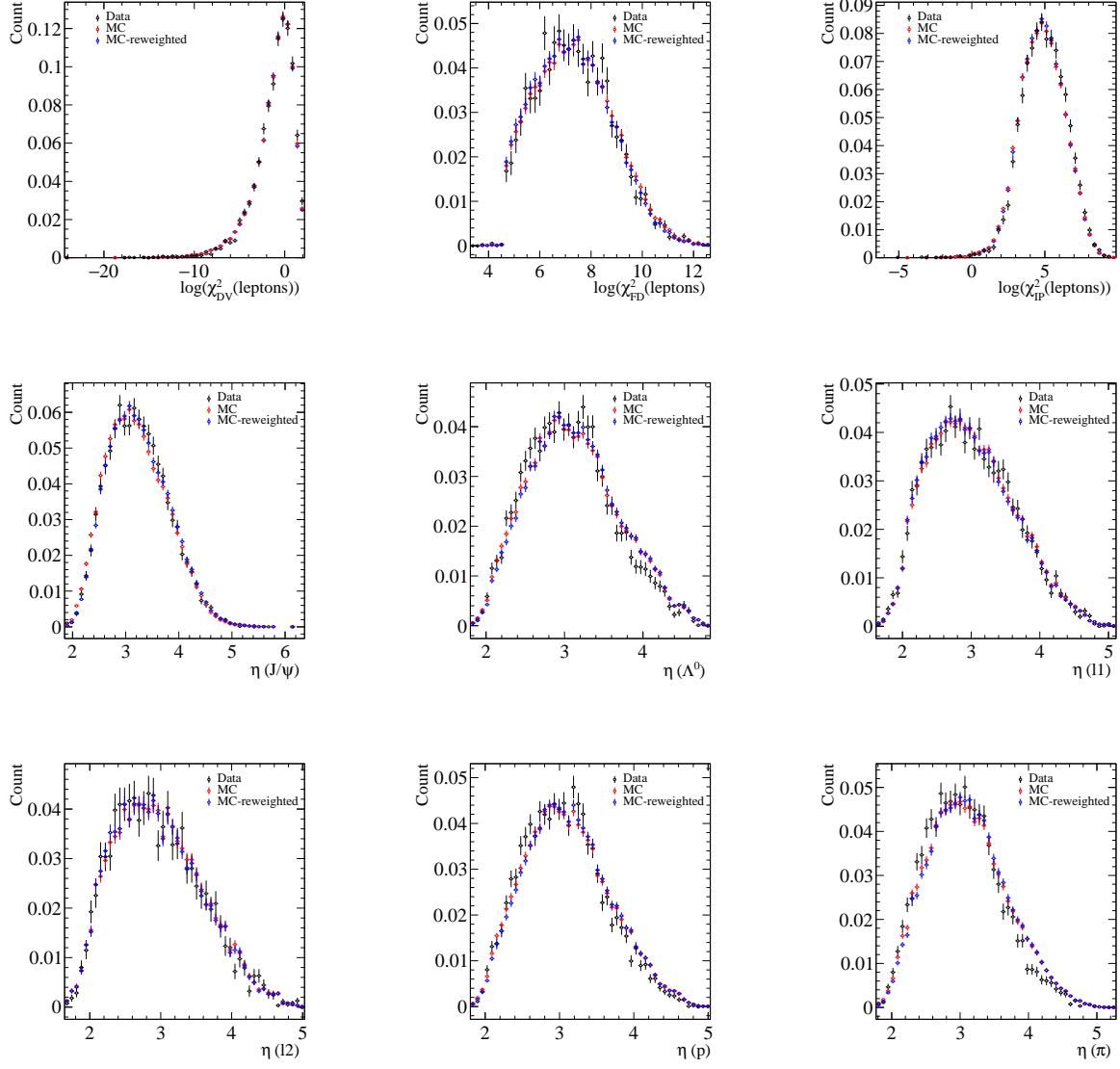


Figure 23: 2018 reweighted variables $\Lambda_b^0 \rightarrow J/\psi \Lambda$

D Reweighted variables $B^0 \rightarrow J/\psi K_S^0$

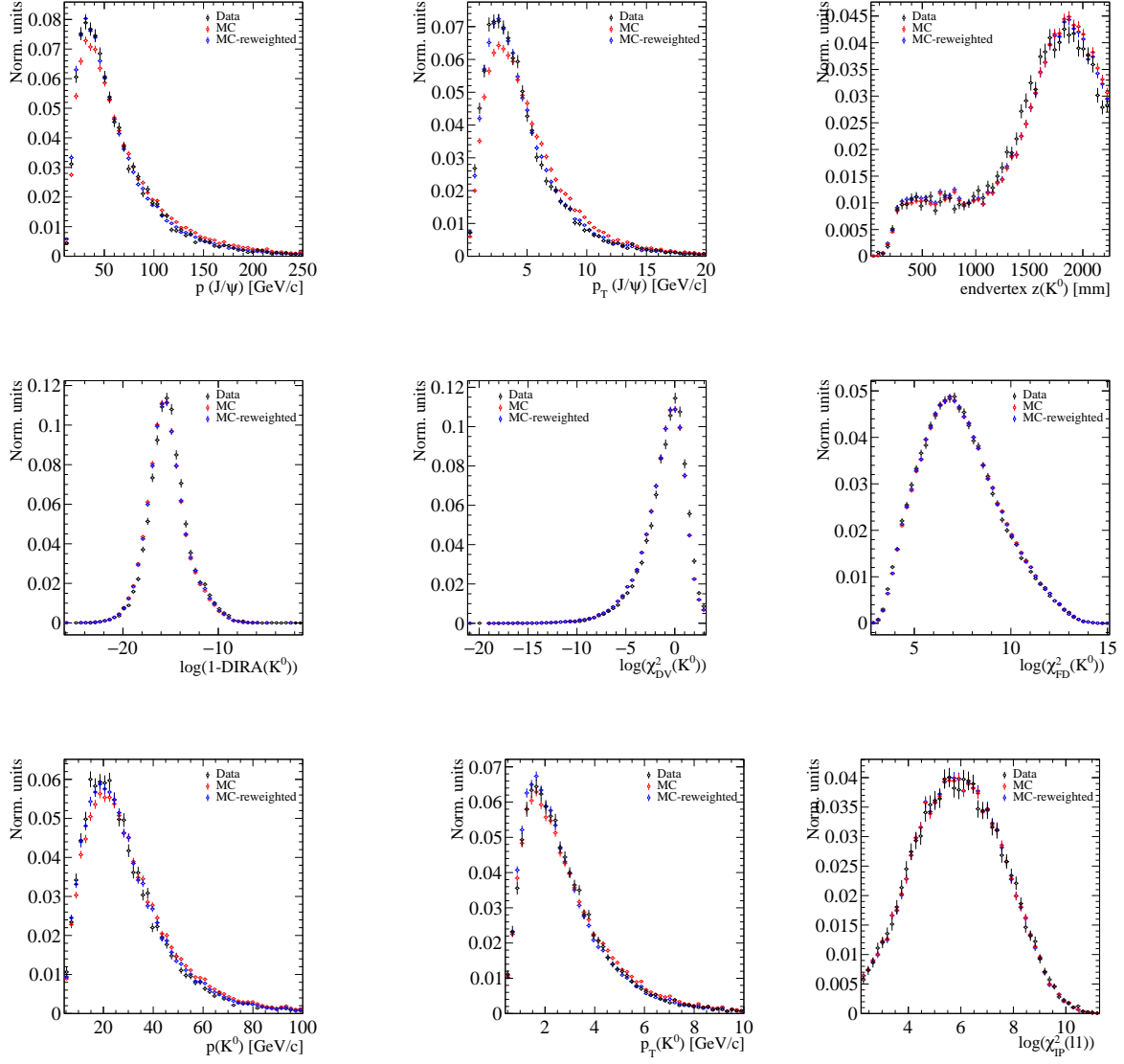


Figure 24: 2018 reweighted variables for $B^0 \rightarrow J/\psi K_S^0$

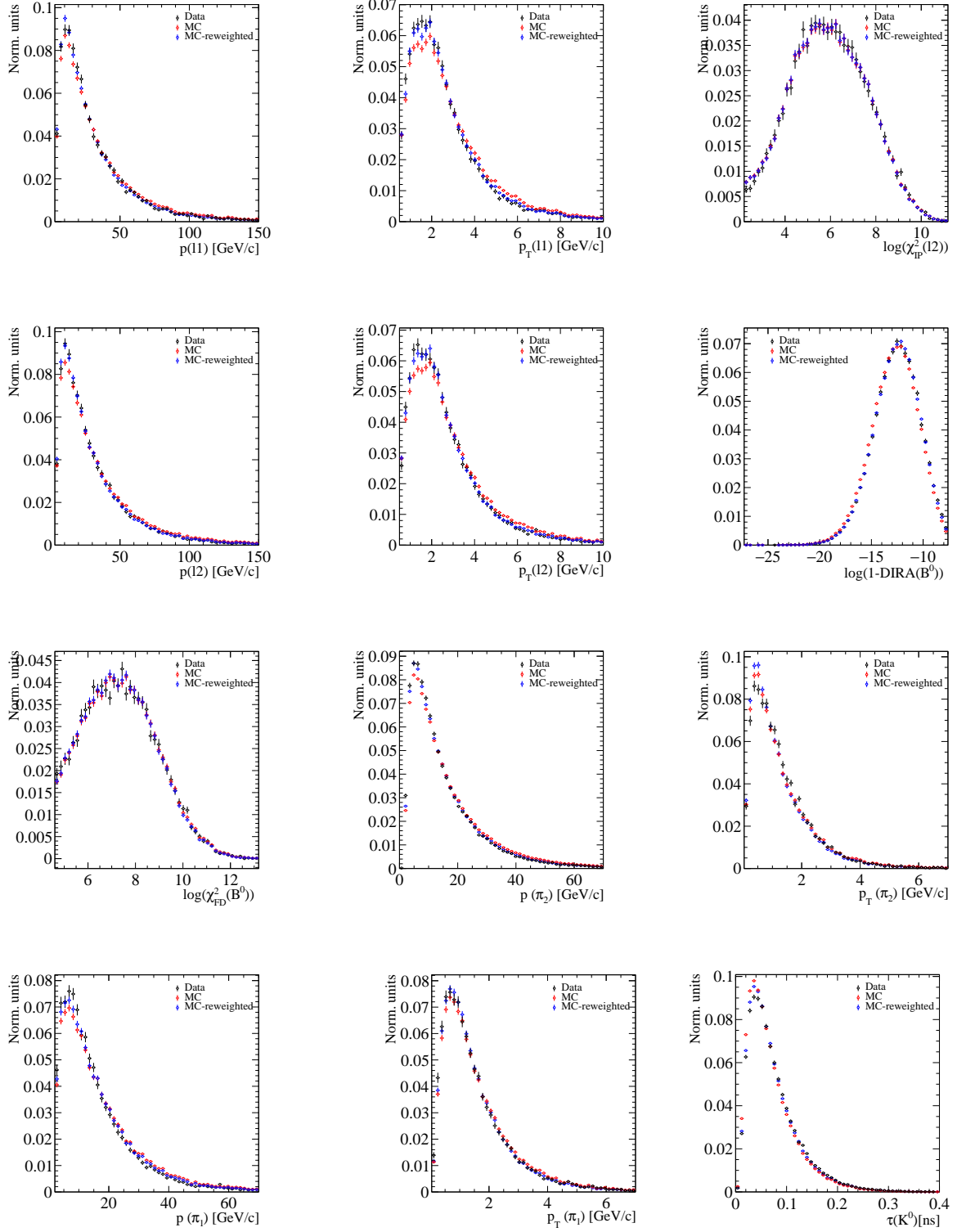


Figure 25: 2018 reweighted variables for $B^0 \rightarrow J/\psi K_S^0$

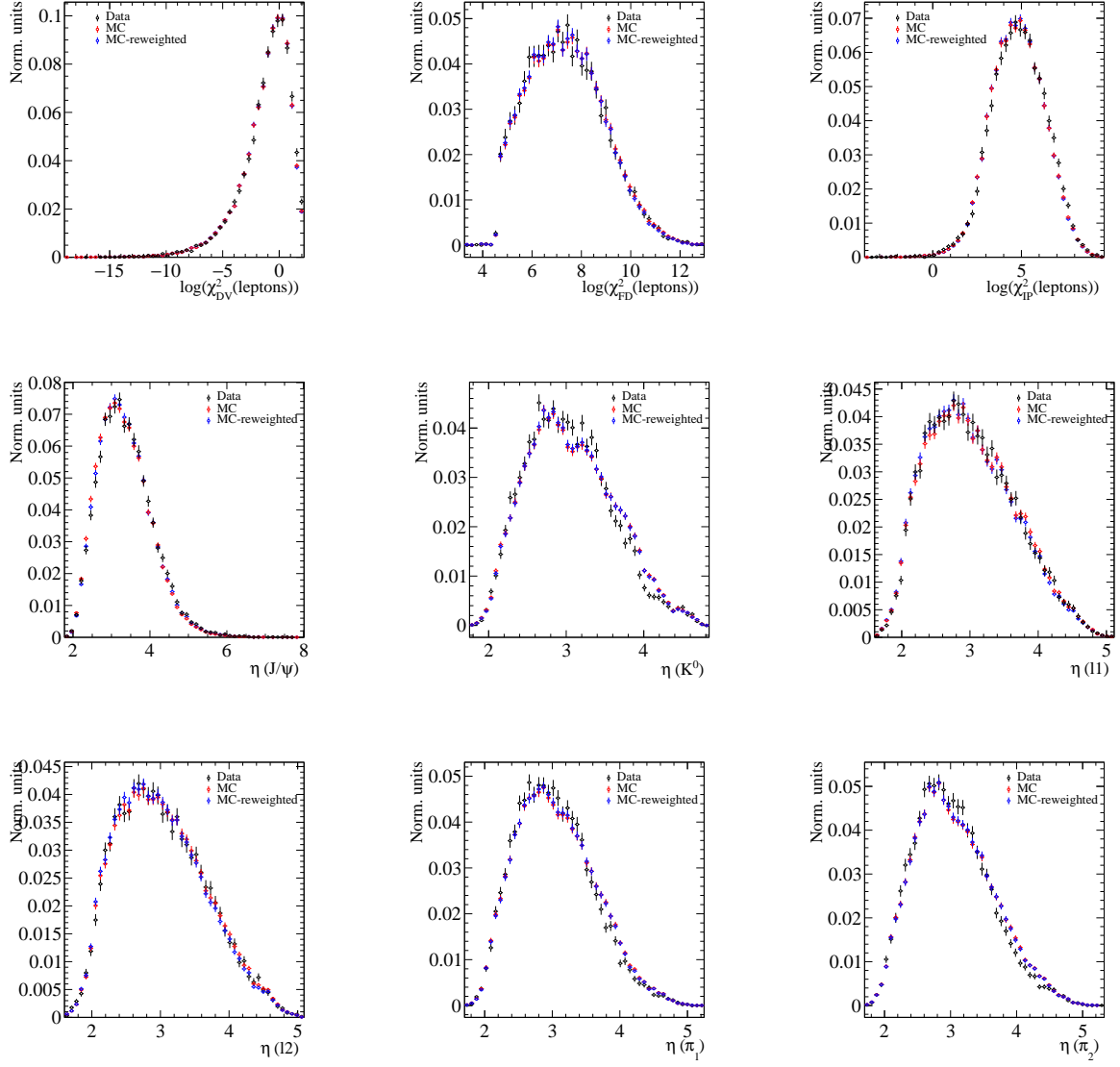


Figure 26: 2018 reweighted variables for $B^0 \rightarrow J/\psi K_S^0$